

1 **High-precision atmospheric oxygen measurement comparisons between a newly built**
2 **CRDS analyzer and existing measurement techniques**

3

4 Tesfaye A. Berhanu^{1,2}, John Hoffnagle², Chris Rella², David Kimhak², Peter Nyfeler¹, Markus
5 Leuenberger¹

6 ¹*Climate and Environmental Physics, Physics Institute and Oeschger Centre for Climate Change Research,*
7 *University of Bern, Bern, Switzerland*

8 ²*Picarro Inc., 3105 Patrick Henry Drive, Santa Clara, CA, USA*

9

10 **Abstract**

11 Carbon dioxide and oxygen are tightly coupled in land-biospheres CO₂ - O₂ exchange
12 processes, while they are not coupled in oceanic exchange. For this reason, atmospheric
13 oxygen measurements can be used to constrain the global carbon cycle, especially oceanic
14 uptake. However, accurately quantifying the small (~1-100 ppm) variations in O₂ is
15 analytically challenging due to the very large atmospheric background which constitutes
16 about 20.9 % (~209500 ppm) of atmospheric air. Here we present a detailed description of the
17 analyzer and its operating principles as well as comprehensive laboratory and field studies for
18 a newly developed high-precision oxygen mixing ratio and isotopic composition analyzer
19 (Picarro G-2207) that is based on cavity ring-down spectroscopy (CRDS). From the
20 laboratory tests, we have calculated a short-term precision (standard error of one-minute O₂
21 mixing ratio measurements) of < 1 ppm for this analyzer based on measurements of eight
22 standard gases analyzed for two hours consecutively. In contrast to the currently existing
23 techniques, the instrument has an excellent long-term stability and therefore a calibration
24 every 12 hours is sufficient to get an overall uncertainty of < 5 ppm. Measurements of

25 ambient air were also conducted at the High-Altitude Research Station, Jungfrauoch and the
26 Beromünster tall tower in Switzerland. At both sites, we observed opposing and diurnally
27 varying CO₂ and O₂ profiles due to different processes such as combustion, photosynthesis
28 and respiration. Based on the combined measurements at Beromünster tower, we determined
29 height dependent O₂:CO₂ oxidation ratios varying between -0.98 to -1.60 , which increase
30 with the height of the tower inlet, possibly due to different source contribution such as natural
31 gas combustion with high oxidation ratio and biological processes which are at the lower end.

32 **1. Introduction**

33 Atmospheric oxygen comprises about 20.9 % of the global atmosphere and in the past decade
34 its concentration decreased at a rate of ~ 20 per meg yr⁻¹ (Keeling and Manning, 2014) mainly
35 associated with the increase in fossil fuel combustion. Measurements of atmospheric O₂ are
36 reported as the ratio to the N₂ concentration and expressed as δ(O₂/N₂) because the variations
37 in the concentrations of other atmospheric gases such as CO₂ can influence the O₂ partial
38 pressure while this ratio is insensitive to these changes in other gases. Atmospheric O₂ is
39 commonly expressed in units of per meg due to its small variability with respect to a large
40 background, where

$$41 \quad \delta \left(\frac{O_2}{N_2} \right) (\text{per meg}) = \left(\frac{\left(\frac{O_2}{N_2} \right)_{\text{sample}}}{\left(\frac{O_2}{N_2} \right)_{\text{reference}}} - 1 \right) \cdot 10^6 \quad (1)$$

42

43 Equation 1 is used to convert oxygen mole fraction changes expressed in ppm (as measured
44 by several techniques such as paramagnetic cell, UV-cell as well as the by the CRDS analyzer
45 presented here) into changes in δO₂/N₂. This is associated with the influence of dilution
46 effects on the mole fractions but not necessarily on the ratios. These conversion difficulties
47 and their expressions in uncertainties are discussed in the Appendix. In contrast to O₂, the

48 global average atmospheric CO₂ mixing ratio increased to 405.0 ppm averaged over 2017
49 since its preindustrial value of 280 ppm (Le Quéré et al., 2017). As the variability of
50 atmospheric oxygen is directly linked to the carbon cycle, both its short and long-term
51 observations can be used to better constrain the carbon cycle. For example, since first
52 suggested by Keeling and Shertz (1992) the long-term trends derived from concurrent
53 measurements of atmospheric CO₂ and O₂ have been widely used to quantify the partitioning
54 of atmospheric CO₂ between the land-biosphere and oceanic sinks (Battle et al., 2000; Goto et
55 al., 2017; Manning and Keeling, 2006; Valentino et al., 2008). This method hinges on the
56 linear coupling between CO₂ and O₂ with an oxidation ratio (OR, defined as the
57 stoichiometric ratio of exchange during various process such as photosynthesis and respiration
58 expressed using α) of 1.1 for the terrestrial biosphere photosynthesis-respiration processes
59 (α_b) and 1.4 for fossil fuel combustion (α_f) while they are decoupled for oceanic processes (α_o
60 = 0). Meanwhile, the short-term variability in atmospheric oxygen can be used to estimate
61 marine biological productivity and air-sea gas exchange (Keeling et al., 1998; Nevison et al.,
62 2012). However, the accuracy of these estimates is primarily linked to the accuracy and
63 precision of atmospheric O₂ measurements and the assumed ORs for the different processes
64 which are highly variable in contrast to atmospheric CO₂ that can be well measured within the
65 precision guidelines set by the Global Atmospheric Watch (GAW) (± 0.1 ppm for the
66 northern hemisphere).

67 Currently there are several, mostly custom built techniques that can measure
68 atmospheric O₂ variations as oxygen concentration based on interferometric, paramagnetic,
69 UV absorption and fuel cell technology (Keeling, 1988a; Manning et al., 1999; Stephens et
70 al., 2007) or as O₂/N₂ ratios to account for the large background effect using gas
71 chromatography with thermal conductivity detector (GC-TCD) or gas chromatography

72 coupled to mass spectrometry (GC-MS) (Bender et al., 1994; Tohjima, 2000). Despite the fact
73 that these techniques have been used for more than two decades, accurate quantification of
74 atmospheric oxygen variability remains challenging primarily because the small ppm-level
75 atmospheric oxygen signal rides on a $\sim 210,000$ ppm background, which places stringent
76 requirements on the precision and drift of the analysis methods especially for continuous
77 monitoring (note that the GAW recommendation for the measurement precision of O_2/N_2 is 2
78 per meg). The techniques listed above struggle to routinely achieve the necessary performance
79 for various reasons, including i) instability over time that requires frequent measurement
80 interruption for calibration, ii) measurement bias with ambient and sample temperature and/or
81 pressure, and/or iii) systematic errors in the measurement due to other atmospheric species.
82 Further, some techniques require the use of consumables and rely on high vacuum, which
83 complicates field deployment.

84 In this manuscript we describe a new high precision oxygen concentration and isotopic
85 composition analyzer by Picarro Inc., Santa Clara, USA (G-2207) based on CRDS
86 technology. Here, we will introduce the analyzer design principles in details, describe the
87 unique features of the analyzer and evaluate its performance based on various independent
88 laboratory and field tests by comparing it with currently existing techniques. Then, we will
89 present and interpret our observations based on field measurements. Finally, we will conclude
90 its overall performance and provide recommendations and possible improvements.

91 **2. Analyzer design principles**

92 The analyzer described here is derived from the Picarro G2000 series of CRDS
93 analyzers. The basic elements have been described elsewhere (Crosson, 2008; Martin et al.,
94 2016; Steig et al., 2014): briefly, the instrument is built around a high-finesse, traveling-wave
95 optical cavity, which is coupled to either of two single-frequency Distributed FeedBack-

96 stabilized semiconductor lasers. One cavity mirror is mounted on a piezoelectric translator
97 (PZT) to allow fine tuning of the cavity resonance frequencies. A semiconductor optical
98 amplifier between the laser sources and the cavity boosts the laser power and serves as a fast-
99 optical switch. The cavity body is constructed of invar and enclosed in a temperature
100 stabilized box ($T = 45^{\circ} \text{C}$, stabilized to approximately 0.01°C) for dimensional and
101 spectroscopic stability. A vacuum pump pulls the gas to be sampled through the cavity and a
102 proportional valve between the cavity and the pump maintains the sample pressure in the
103 cavity at a value of 340 hPa, with variations on the order of 1 Pa. The instrument has a
104 wavelength monitor, based upon measurements of interference fringes from a solid etalon,
105 which is used to control the laser wavelength by adjusting the laser temperature and current.
106 The wavelength monitor is a fiber-coupled device located between the laser and the cavity. A
107 fraction of the beam from the input fiber is collected using a beam splitter for the wavelength
108 measurement and the remaining power is collected in the output fiber. A high-speed
109 photodiode monitors the optical power emerging from the cavity. The instrument's data
110 acquisition system is used to sweep the laser frequency over the spectral feature to be
111 measured, modulates the laser output to initiate ring-downs, and fits the ring-down signal to
112 an exponential function to generate a spectrogram of optical loss versus laser frequency. For
113 this instrument the empty cavity ring-down time constant is about $39 \mu\text{s}$. Subsequent program
114 modules compare the measured loss spectrum to a spectral model, using non-linear least-
115 squares fitting (Press et al., 1986) to find the best-fit model parameters and thereby obtain a
116 quantitative measure of the absorption due to the target molecule, and finally apply a
117 calibration factor to the optical absorption to deduce the molecular concentration. When
118 operating in its normal gas analysis mode, the instrument acquires about 200-300 ring-downs

119 per second and achieves a noise equivalent absorption of typically about $10^{-11} \text{ cm}^{-1} \text{ Hz}^{-1/2}$,
120 with some variation between instruments.

121 The primary goal when designing this analyzer was to measure the molecular oxygen
122 concentration with few-per-meg level precision and stability. In this context operational
123 stability is as important as signal-to-noise. Our experience has been that the most stable
124 operation of the analyzer is achieved when the optical phase length of the cavity is held as
125 nearly constant as possible. In this case the free spectral range (FSR, 0.0206 cm^{-1}) of the
126 temperature stabilized, invar ring-down cavity provides a better optical frequency standard
127 than the etalon-based wavelength monitor, which in turn allows more consistent
128 measurements of absorption line width and integrated absorption line intensity (Steig et al.,
129 2014). For a small, field-deployable instrument, it is not practical to stabilize the absolute
130 frequencies of the cavity modes to an optical frequency standard (Hodges et al., 2004) but the
131 oxygen lines themselves, under conditions of constant temperature and pressure, provide an
132 adequate frequency reference. The oxygen spectrum was also used to calibrate the FSR, by
133 comparing a wide (approximately 10 cm^{-1}) FSR-spaced spectrum with the Hitran database
134 (Rothman et al., 2013).

135 To determine molecular oxygen concentration, the analyzer measures absorption of the
136 Q13Q13 component of the $a^1\Delta_g \leftarrow X^3\Sigma_g^-$ band, at $7878.805547 \text{ cm}^{-1}$, according to the latest
137 edition of Hitran (Gordon et al., 2017). This is one of the strongest near-infrared lines of
138 oxygen, well separated from other oxygen lines, and reasonably free of spectral interference
139 from water, carbon dioxide, methane, and other constituents of clean air. The spectral model
140 for this line was developed using reference spectra of clean, dry, synthetic air that were
141 acquired with the same hardware as in the field-deployable analyzer, but with special-purpose
142 software that allows it to operate as a more general spectrometer.

143 Recently, considerable work has been done to advance the understanding of spectral
144 line shapes and to define functional representations that better describe the processes that
145 determine spectral line shapes than does the Voigt model (Hartmann et al., 2008; Tennyson et
146 al., 2014, Tran et al., 2019). Line shape studies have been published for the 1.27 μm band of
147 O_2 (Fleisher et al., 2015; Lamouroux et al., 2014), though not to our knowledge for the Q
148 branch. The apparatus used here is not capable of spectroscopic studies of comparable
149 precision; the absolute temperature and pressure monitoring and especially the frequency
150 metrology are far too crude for that purpose. Our goal is merely to define a simple model of
151 the Q13Q13 line that is adequate for least-squares retrievals of the O_2 absorption under the
152 limited range of conditions (stabilized temperature and pressure) that the operational analyzer
153 experiences in the field. The CRDS analyzers use the Galatry function (Varghese and Hanson,
154 1984), which is distinctly better than the Voigt and still easily and quickly evaluated for line
155 shape modeling. Ultimately, the usefulness of the spectral model is to be evaluated by the
156 precision and stability of the O_2 measurements when compared with established techniques.
157 For spectral model development, this spectrometer has the drawback that the cavity FSR, is
158 too large to reveal much detail of the absorption line shape, even with the simplifying
159 assumption of a Galatry line shape. We therefore acquired a set of four interleaved spectra,
160 with the PZT-actuated mirror moved to offset the cavity modes of the individual FSR-spaced
161 spectra by one-fourth of an FSR. The precise offsets were determined from fits to the strong
162 and well-isolated O_2 lines in the spectra. From the consistency of the fitted line centers, we
163 estimate that the positioning of the interleaved spectra was accurate to approximately 10
164 MHz. The spectrum of the Q13Q13 line acquired in this manner is shown in Figure 1,
165 together with the best-fit Galatry function. It stands out that the residuals are largely odd in
166 detuning from the line center: this shows the limitations of the Galatry model in this case,

167 since the Galatry function is purely even about the line center. The shape of the absorption
168 line in this model is specified by two dimensionless parameters: the collisional broadening
169 parameter

$$170 \quad \gamma = \gamma / \sigma_D \quad (2)$$

171 and the collisional narrowing parameter

$$172 \quad z = \beta / \sigma_D \quad (3)$$

173 where γ is the frequency of broadening transitions, β is the velocity change collision rate, and
174 σ_D is the 1/e Doppler half-width of the transition, given by

$$175 \quad \sigma_D = \nu_0 (2k_B T / M c^2)^{1/2} \quad (4)$$

176 where ν_0 is the transition frequency, k_B is Boltzmann's constant ($J \cdot K^{-1}$), T is the sample
177 temperature (K), M is the molecular mass (amu), and c is the speed of light (m/s). Figure 2
178 shows the values of γ and z obtained from spectra acquired in the same way as Figure 1, as a
179 function of cavity pressure. The values depend linearly on pressure, as expected from the
180 Galatry model, but the unconstrained linear fits do not go precisely through the origin. It is
181 not clear whether this represents a breakdown of the Galatry model or simply reflects the
182 limited quality of the data set. The slope of γ can be converted to an air-broadened collisional
183 width $\gamma_{\text{air}} = 0.0442 \text{ cm}^{-1}/\text{atm}$, which agrees with the Hitran value of $0.0460 \text{ cm}^{-1}/\text{atm}$ (Gordon
184 et al., 2016) to within the uncertainty estimate stated by Hitran (uncertainty code 4 for γ_{air}
185 corresponding to 10% --20% relative uncertainty). The slope of z can be interpreted in terms of
186 the optical diffusion coefficient (Fleisher et al., 2015), yielding $D = 0.285 \text{ cm}^2 \text{ s}^{-1}$, compared
187 to the literature value of $0.233 \text{ cm}^2 \text{ s}^{-1}$ for O_2 in air at $45 \text{ }^\circ\text{C}$ (Marrero and Mason, 1972).
188 Although the anticipated use of the analyzer is for ambient air samples having a very small
189 range of O_2 concentrations, we did investigate the variation of the line shape in binary
190 mixtures of O_2 and N_2 shown in Figure 3. The error bars are taken from the output of the

191 Levenberg-Marquardt fitting routine (Press et al., 1992). The dependence of the collisional
192 broadening parameter z on O_2 mole fraction was considered too small to be significant, but
193 the variation in y was used in the subsequent analysis of the air samples. Note that Wójtewicz
194 et al. (Wójtewicz et al., 2014) also found collisional broadening coefficients for nitrogen to be
195 slightly larger than for oxygen in measurements of one O_2 line in the B-band.

196 The primary goal in designing the analyzer was to achieve high enough precision to
197 make meaningful measurements of O_2 in clean atmospheric samples. Although the current
198 best practice for such high-precision measurements is to work with dried samples, we decided
199 to include high precision measurements of water vapor. There were two reasons for this
200 decision: one is to serve as a monitor for residual water vapor, which is difficult to remove
201 completely from the ring-down cavity and associated sample handling hardware, and the
202 second and more ambitious reason was to see how well the effect of water vapor could be
203 corrected for measurements of undried ambient air. While it was considered unlikely that
204 measurements of undried air could compete in accuracy with those of dried air, it might be
205 possible to correct for water vapor well enough to enable useful measurements in some
206 circumstances without the expense and inconvenience of drying the sample. For this purpose,
207 a second laser was added, which probes the $7_{1,6} \rightarrow 8_{4,5}$ component of the $2\nu_3$ band of water
208 vapor, at of $7816.75210 \text{ cm}^{-1}$ (Gordon et al., 2017). The Galatry model was used to fit spectra
209 of synthetic air humidified to various levels of water vapor concentration. These fits also
210 included two other nearby, very weak water lines, with intensities less than 1% of the strong
211 transition, in order that their absorption should not perturb the line shape of the main
212 transition. Results for the shape of the $7816.75210 \text{ cm}^{-1}$ line are shown in Figure 4. At the
213 level that we can measure, only the y -parameter has a meaningful variation with water
214 concentration. From the linear fit one obtains a pressure broadening coefficient for air, $\gamma_{\text{air}} =$

215 0.0752 cm⁻¹/atm, in reasonable agreement with the Hitran value $\gamma_{\text{air}} = 0.0787$ cm⁻¹/atm
216 (Gordon et al., 2017), and a self-broadening coefficient $\gamma_{\text{self}} = 0.413$ cm⁻¹/atm, to be compared
217 with the Hitran value $\gamma_{\text{self}} = 0.366$ cm⁻¹/atm. Since the uncertainty estimate for the Hitran
218 values is 10 % to 20 %, this level of agreement seems reasonable.

219 We also looked at absorption from water near the Q13Q13 absorption line of O₂.
220 These spectra were measured in a background of pure nitrogen to reveal the very weak lines
221 interfering with the O₂ measurement. Without the strong O₂ lines, it was impossible to
222 interleave FSR-spaced spectra, so in this case the frequency axis comes from the analyzer's
223 wavelength monitor. The upper panel of Figure 5 shows the spectrum of saturated water vapor
224 in nitrogen, together with a fit to a Voigt model of the molecular lines. The measurement was
225 made at a pressure of 340 hPa and temperature of 45° C. The main features are the Q13Q13 line
226 from trace contamination of oxygen in the sample and several lines that arise from normal water
227 (¹H₂¹⁶O) and deuterated water (¹H²H¹⁶O also abbreviated HDO). The lower panel of Figure 5 shows
228 the lines tabulated in Hitran. Immediately after the data in Figure 5 were acquired,
229 measurements were also made at 7816.85210 cm⁻¹, to establish the relationship between the
230 absorption strengths in the two spectral regions. The relative intensities of the H₂O and HDO
231 lines change with variations in the isotopic composition of the water, but fortunately the direct
232 interference with the oxygen Q13Q13 lines comes entirely from the H₂O isotopologue, with
233 the strongest HDO line being separated by approximately 8 line widths (FWHM) from the
234 Q13Q13 line. Hitran simulations for molecules other than water that are expected to be
235 present in clean, ambient air indicate that direct interference with the Q13Q13 line should be
236 negligible at the level of precision considered here. In the case of CO₂, the dilution of oxygen
237 due to 400 ppm of CO₂ is significant, and larger than any direct spectral interference.

238 Finally, we investigated the influence of water vapor on the shape of the O₂ Q13Q13
239 line. Switching between the two lasers sources, we acquired FSR-spaced spectra of
240 humidified synthetic air, alternately covering the 7817 cm⁻¹ and 7878 cm⁻¹ regions. Individual
241 spectra were acquired in less than 2 s, so changes in water vapor concentration between
242 spectra were small. These spectra, with frequency resolution of 0.0206 cm⁻¹, were analyzed by
243 nonlinear least-squares fitting with the following spectral models: the 7817 cm⁻¹ spectra were
244 modeled as the sum of an empty-cavity baseline having an adjustable offset level and slope
245 and the water spectrum is modeled with three peaks: one strong line and two weak perturbers.
246 The molecular absorption of the main peak was expressed as an adjustable amplitude, A_w ,
247 multiplying a dimensionless, area-normalized Galatry function (Varghese and Hanson, 1984).
248 The weak perturbers were modeled by Voigt profiles with amplitudes and line widths that
249 were constrained to be in fixed proportions to the strong line, and therefore added no new
250 degrees of freedom to the fitting procedure. Since the amplitude A_w multiplies an area-
251 normalized shape function, it is essentially equivalent to the area of the absorption line, to the
252 extent that the Galatry model provides a valid description of the line shape. The Doppler
253 width of the Galatry function was fixed based on the measured cell temperature, the y -
254 parameter was allowed to vary, and the z -parameter was constrained to be proportional to y ,
255 based on measurements summarized in Figure 2. In addition, the center frequency of the
256 Galatry function was adjusted to match the data set, giving a total of five free parameters for
257 this fit. The 7878 cm⁻¹ spectra were modeled with an adjustable baseline offset and slope and
258 molecular absorption amplitude, A_{O_2} , describing the Q13Q13 O₂ line. Here, too, the y -
259 parameter and line center position of the O₂ lines were allowed to adjust, and the z -parameter
260 was constrained to be proportional to y . The weak water lines interfering with oxygen
261 absorption were included in the model, but with no additional free parameters; rather the

262 amplitudes were preset based on the measured water absorption at 7817 cm^{-1} and the
263 previously determined amplitude relationships between the water lines. This procedure does
264 not account for variations in HDO abundance, which may introduce some systematic error
265 into the water vapor correction for samples of unusual isotopic composition, but it should
266 accurately model the most important lines that interfere with the oxygen measurement.
267 Collisional broadening of the Q13Q13 O_2 line by water vapor is shown in Figure 6. From the
268 linear fit one obtains a coefficient for collisional broadening of the Q13Q13 line by water
269 vapor of $\gamma_{\text{water}} = 0.0442\text{ cm}^{-1}/\text{atm}$ at $45\text{ }^\circ\text{C}$. Recently, parameters describing broadening of
270 oxygen lines by water vapor, obtained by empirical modeling of selected experimental
271 data, were added to the Hitran data base (Tan et al., In review). The new Hitran entries predict
272 a value of $0.0486\text{ cm}^{-1}/\text{atm}$ at $45\text{ }^\circ\text{C}$, which is in agreement with our measurement within the
273 5-10% uncertainty attributed by Hitran to the broadening parameter. The alternating
274 measurements at 7817 cm^{-1} and 7878 cm^{-1} also calibrated the relationship between water mole
275 fraction and the absorption at 7817 cm^{-1} , using a dilution analysis described by Filges et al.
276 (2018), who showed that the results obtained this way agree well with water vapor fractions
277 measured with a conventional hygrometer. Figure 7 shows the measured amplitudes of the
278 water and oxygen lines for samples of variable humidity. Since the air came from a tank of
279 constant composition, the oxygen concentration changes due to dilution of oxygen when
280 water is added. Assuming that this is the sole cause of the change in measured absorption,
281 since the line shapes were being constantly adjusted to account for changes in collisional
282 broadening, it is straightforward to deduce the relation between the water fraction and the
283 absorption amplitude. This calibration was used to generate the water fraction axes in Figures
284 4 and 6. We note that we did not take particular care to control or measure the quantity of
285 dissolved gases, especially oxygen and carbon dioxide, in the water used for this experiment.

286 While these gases would not significantly affect the water calibration, they may affect the
287 water vapor correction of the oxygen measurement at the ppm level. More work needs to be
288 done to investigate the water vapor correction of the oxygen measurement.

289 The observations described above were used to design a method to measure oxygen
290 concentration in ambient air. Gas from the inlet to the analyzer is drawn through the cavity at
291 a rate of about 100 sccm (standard cubic centimeter per minute) and the conditions in the
292 cavity are held stable at 340 hPa and 45°C. In its analysis mode the analyzer alternately
293 measures ring-downs in the 7817 cm^{-1} and 7878 cm^{-1} regions. At 7878 cm^{-1} measurements are
294 made at 11 different frequencies, spaced by one FSR of the cavity and centered at the peak of
295 the Q13Q13 line. Multiple ring-down measurements are made to improve the precision of the
296 loss determination, with a total of 305 ring-downs allocated to one spectrum. In the 7817 cm^{-1}
297 region measurements are also made at 11 distinct frequencies at FSR spacings. Only 35 ring-
298 downs are allocated to this spectral region, since the measurement of O_2 is much more
299 important than water vapor. The data sets are analysed using a Levenberg-Marquardt fitting
300 routine, which adjusts five free parameters in each region to find the best agreement to a
301 spectral model based on Galatry line shapes, as described above. One of the outputs of the
302 7878 cm^{-1} fit is the frequency offset of the FSR grid from the center of the Q13Q13 line. This
303 information is used to adjust the position of the PZT actuated mirror to keep the
304 measurements centered on the line, effectively stabilizing the optical path length of the cavity
305 to the frequency of the O_2 line. The reported water fraction is obtained by multiplying the
306 fitted amplitude of the water line by a calibration constant derived from the dilution
307 experiment as explained above. For the O_2 fraction a slightly more complicated procedure is
308 followed. It was observed that the least-squares fitting of the data gives highly correlated
309 results for the amplitude of the absorption line and the line width parameter γ . The correlation

310 may be due in part to covariance of the fitted amplitude (proportional to line area) and line
311 width (Press et al., 1992) and it may also have a contribution from pressure variations that the
312 pressure sensor is unable to detect. The ratio A_{O_2}/y can be determined from the fit much more
313 precisely than A_{O_2} alone and so gives a more sensitive measurement of molecular absorption.
314 It also has the advantage of being independent of sample pressure, to the extent that the
315 Galatry model applies (Figure 2). However, using the ratio A_{O_2}/y as a metric for absorption
316 adds more complications if measurements are to be made over a range of O_2 and water
317 concentrations, because the O_2/N_2 ratio and the water concentration affect the line width
318 independently of pressure and O_2 concentration alone. To minimize systematic errors due to
319 these broadening effects, we define a nominal y -parameter based on the measured amplitudes
320 of the O_2 and water lines and the line broadening dependences shown in Figures 3 and 4. The
321 measured ratio A_{O_2}/y is multiplied by the nominal y to obtain a quantity that is ideally
322 independent of pressure and water concentration, and this is the quantity that is multiplied by
323 a calibration constant to give the reported O_2 fraction. In addition, a dry mole fraction is
324 reported for O_2 , defined as the directly measured mole fraction corrected for water dilution.

325 The main goal in developing this instrument was to make high precision
326 measurements of O_2 mole fraction, based on absorption by the dominant $^{16}O_2$ isotopologue.
327 The absorption lines of the rarer isotopologues are also present nearby, so a mode of operation
328 was included in which one laser is scanned over neighboring lines of $^{16}O_2$ and $^{16}O^{18}O$ and the
329 ratio of amplitudes is used to derive an isotopic ratio, reported in the usual delta notation. In
330 this case the operating pressure was reduced to 160 hPa to improve the resolution of the
331 nearby lines. The lines measured were the Q3Q3 line of $^{16}O_2$, at $7882.18670\text{ cm}^{-1}$, and the
332 Q9Q9 line of $^{16}O^{18}O$, at $7882.050155\text{ cm}^{-1}$. The measurement procedure is very much like
333 that for the O_2 fraction measurement, so it will not be described in detail, only the main

334 differences will be noted. One is that in determining an isotopic ratio, normalizing absorption
335 amplitudes by line widths does not provide any advantage, instead we simply take the ratio of
336 amplitudes to compute delta. Although the Q9Q9 line and its neighbor Q8Q8 are the strongest
337 ones in this band, absorption by $^{16}\text{O}^{18}\text{O}$ is still very weak, only about $5 \times 10^{-9} \text{ cm}^{-1}$ at the line
338 center under the conditions we used. The signal-to-noise that can be achieved with this
339 analyzer is not adequate to determine both the amplitude and the width of the $^{16}\text{O}^{18}\text{O}$ line with
340 useful precision, so in the fitting step the y-parameter of the $^{16}\text{O}^{18}\text{O}$ line is constrained to be a
341 constant factor times the fitted y-parameter for the $^{16}\text{O}_2$ line. Additionally, because of the
342 weakness of the rare isotopologue absorption, the majority of ring-downs in each spectrum is
343 devoted to measuring $^{16}\text{O}^{18}\text{O}$ i.e. 232 ring-downs in each spectrum versus only 40 for $^{16}\text{O}_2$.
344 This implies that the mole fraction measurement in the isotopic mode is much less precise
345 than when the analyzer measures the Q13Q13 line alone.

346 **3. Results and Discussions**

347 **3.1. Laboratory tests at Picarro, Santa Clara**

348 3.1.1. Temperature and pressure sensitivity

349 One set of tests was done to determine how well the goal was met of minimizing the
350 susceptibility of the concentration measurements to noise or drift of the sample temperature
351 and pressure. For these tests the analyzer sampled dry synthetic air from a tank and the
352 temperature and pressure setpoints of the cavity were adjusted upward and downward from
353 the nominal values, to obtain an estimate of the differential response. We express the
354 sensitivity to experimental conditions in relative form, that is the derivative with respect to
355 temperature or pressure divided by the signal under nominal conditions.

356 From these experiments, we determined a temperature sensitivity of $-2.1 \times 10^{-4} \text{ K}^{-1}$ and
357 a pressure sensitivity of $+9.8 \times 10^{-6} \text{ hPa}^{-1}$. The temperature sensitivity is somewhat larger than

358 expected based on a calculation using Hitran data to estimate the temperature dependences of
359 all the quantities that go into the measured absorption of the Q13Q13 line. The pressure
360 sensitivity is strikingly small, indicating a good cancelation of the pressure dependence of
361 absorption amplitude and line width. Both temperature and pressure sensitivities are small
362 enough to have a negligible effect on short-term precision of measurements made with the
363 stabilized ring-down cavity, though long-term drifts in the sensors are always a matter of
364 concern.

365 3.1.2. Measurement precision and drift

366 Measurement precision was evaluated by analyzing synthetic air containing nominal
367 atmospheric concentrations of CO₂ and CH₄ from an aluminum Luxfer cylinder over a period
368 of several days. The tank, oriented horizontally and thermally insulated (though not
369 controlled), was connected directly to the instrument (S/N TADS2001) with a 2-stage
370 pressure regulator and stainless-steel tubing with an additional orifice to about 55 sccm. For
371 the isotopic mode of operation, the precision of the measurement was also tested by making
372 repeated measurements from a tank of clean, dry synthetic air.

373 Figure 8 shows the time series of the precision test data, displaying the reported
374 oxygen concentration, the height of the oxygen absorption peak, the width of the oxygen
375 absorption peak and the ambient temperature. The residual error of the analyzer, although
376 small, is nevertheless significant given the stringent targets set forth by the WMO-GAW
377 program. Possible sources of error include: temperature drifts due to sensor drift or gradients;
378 pressure errors due to sensor drift; optical artifacts such as parasitic reflections, higher order
379 cavity mode excitation, and/or loss nonlinearity that can distort the reported oxygen spectrum.
380 More work is required to identify and eliminate these small drifts.

381 The Allan standard deviation of the reported O₂ fraction is shown in the Allan-Werle
382 plot in Figure 9. The ordinate on this plot is the square root of the Allan variance of reported
383 mole fraction, so 1 ppm in these units corresponds to about 5 per meg in the ratio of O₂/ N₂.
384 The precision of averaged measurements improves as $\tau^{-1/2}$ for approximately 5000 s and
385 reaches 1 ppm in less than 10 minutes and remains below 1 ppm for time scales on the order
386 of about 1 hour (τ is the averaging time which is the abscissa of the Allan-Werle plot).

387 Figure 10 shows the precision of $\delta(^{18}\text{O})$ (uncalibrated) derived from the ratio of lines
388 measured at 7882 cm⁻¹. Because of the weak signal from the ¹⁶O¹⁸O line, it is necessary to
389 average for more than 20 seconds or more to achieve 1‰ precision on the isotopic ratio. As
390 for the concentration measurement, averaging improves the measurement precision for time
391 scales up to about 1 hour.

392 **3.2. Laboratory measurements at the University of Bern**

393 3.2.1. Measurements of standard gases

394 The performance of the instrument was tested by analyzing eight standard gases with
395 precisely known CO₂ and O₂ compositions (Table 1) using the CRDS analyzer and comparing
396 it to parallel measurements with a paramagnetic oxygen sensor (PM1155 oxygen transducer,
397 Servomex Ltd, UK) embedded to a commercially available fuel cell oxygen analyzer
398 (OXZILLA II, Sable Systems International, USA) (Sturm et al., 2006) as well as with an
399 isotope ratio mass spectrometer (IRMS, Finnigan Delta^{Plus}XP). The design of the
400 measurement set-up is shown in Figure 11. Standard gases were directly connected to the
401 pressure controlling unit, and a multi-port valve (V2) was used to select among the standard
402 gases. Flow from each cylinder was adjusted to about 120 sccm which was eventually
403 directed to a selection valve (V1), allowing switching between ambient air and standard gases.
404 Flow towards and out of the fuel cell analyzer was controlled by the pressure controlling unit.

405 The O₂ mixing ratio of this incoming gas was first measured on the Paramagnetic O₂ sensor
406 and then directed towards a non-dispersive infrared analyzer (NDIR) (Li-7000, LICOR, USA)
407 for measuring CO₂ and H₂O. The outflow from this analyzer (100 sccm) returns to the
408 pressure controlling unit and was eventually divided between the CRDS analyzer (which uses
409 about 75-80 sccm) and the IRMS (~ 20 sccm) via a Tee-junction. Each cylinder was measured
410 for two hours in each system controlled by a LabView program.

411 First, we investigated the influence of this Tee-junction, which splits the gas flow
412 between the CRDS and the IRMS, on the measured O₂ values. Manning (2001) showed that
413 the fractionation of O₂ in the presence of a Tee-Junction is strongly dependent on the splitting
414 ratios as well as temperature and pressure gradients. Hence, we measured and compared the
415 O₂ mixing ratios of two standard gases (CA07045 and CA060943) in two cases: i) in the
416 presence of a Tee-junction with different CRDS to IRMS splitting ratios and ii) without a
417 Tee-junction so that all gas flow is directed towards the CRDS analyzer. The splitting ratios in
418 these test experiments vary from 1:1 to 1:100, and reversed to change the major flow direction
419 either to the CRDS or the IRMS. Note that the experimental condition in this manuscript is
420 with a 4:1 splitting ratio (i.e. ~ 80 sccm towards the CRDS analyzer and ~ 20 sccm towards
421 the IRMS).

422 In the cases of the smaller splitting ratios (1:1, 1:4 and 4:1), which are relevant for the
423 results presented in this study, only minor differences in the measured O₂ mixing ratios were
424 observed when compared to case ii (i.e. without a Tee-junction). For these two cylinders
425 measured, the average differences in these cases were about 0.5 ppm, calculated as the mean
426 of the differences in the raw O₂ measurements of the last 60 seconds. The negligible
427 fractionation can indeed be the result of smaller splitting ratios while strong influence is
428 usually expected in case of larger splitting ratios (Stephens et al., 2007). For higher splitting

429 ratios, the result seems inconclusive without any dependence on the ratios due to the strong
430 decline in the cylinder temperature (specifically at the pressure gauge) caused by higher flow
431 to achieve the higher splitting ratios (as high as 1:100). Hence, these tests need to be
432 conducted in a temperature-controlled condition and the results could not be discussed in this
433 manuscript.

434 Figure 12 shows the standard gas measurements for the seven cylinders with known
435 CO₂ and O₂ mixing ratios (Table 1) using both the CRDS and the Paramagnetic analyzers.
436 Standard eight, which has too high O₂, is not shown in the figure as the figure is zoomed-in to
437 better illustrate the change in O₂ for the remaining cylinders. While the first five cylinders
438 contain O₂ and CO₂ mole fractions comparable to ambient air values, standards 6 & 8 had
439 either very low or very high O₂, respectively. In addition, standards 6 and 7 have very low and
440 very high CO₂ mixing ratios. Note that due to its very high CO₂ content (~ 2700 ppm),
441 standard 7 was not measured on the IRMS and hence the O₂ mixing ratio is unknown. The
442 measured mixing ratios for the six standard gases measured with the two systems are in very
443 good agreement while cylinder 7 showed an opposing signal for the two analyzers compared
444 to standard 6 (Figure 12). While the Paramagnetic analyzer showed a higher O₂ mixing ratio,
445 the values from the CRDS analyzer are lower in O₂. This can be associated with the very high
446 CO₂ mixing ratio in standard 7, which leads to a strong dilution effect in the CRDS analyzer
447 as it does not include any correction function for dilution effect from CO₂. However, such
448 high CO₂ mixing ratios may not be that important for most atmospheric research. Yet, it
449 should be considered to include a parallel CO₂ mixing ratios measurement to the instrument
450 as it will further improve the accuracy. This would be especially important for biological or
451 physiological studies where a wide range of CO₂ and O₂ concentrations must be expected.

452 The measurement precision of the CRDS analyzer was calculated as the standard error
453 of the mean i.e. the standard deviation ($1-\sigma$) of the last 1-minute raw measurements divided
454 by the square root of the number of measurements ($n = 60$), and for all these cylinders the
455 values are usually between 0.5 ppm to 0.7 ppm. For parallel measurements of these cylinders
456 using a Paramagnetic analyzer, we obtained a precision of about 1 ppm, calculated exactly the
457 same way.

458 We also made a correlation plot to see which of the two instruments are in better
459 agreement with the assigned values based on IRMS measurements for the individual
460 cylinders. While similar correlation coefficients were observed for both analyzers, different
461 slopes were calculated (Fig. A.1). This is due to the fact that the IRMS measures the O₂ to N₂
462 ratio ($\delta(\text{O}_2/\text{N}_2)$) in per meg, while the CRDS and the Paramagnetic analyzers provide non-
463 calibrated O₂ mixing ratios in units of ppm and per meg, respectively. If we exclude the two
464 standard gases with the highest and lowest O₂ mixing ratios (standards 7 and 8) that are
465 subjected to strong dilution effects, both the slope and the r^2 values decrease from those
466 shown in Figure A.1. But this decrease is larger in the case of the Paramagnetic
467 measurements, implying a slightly better linearity of the CRDS analyzer.

468 Furthermore, the slope between the IRMS and CRDS O₂ values in Figure A1
469 corresponds to 5.78 per meg ppm⁻¹, significantly larger than the conversion factor of 4.78 per
470 meg ppm⁻¹ as derived from equation 1 assuming constant N₂ content. This higher slope is due
471 to dilution effect originating from any gas component change (Δ , given in ppm) on all air
472 components of air samples, which has not been corrected for the CRDS values. When
473 accounting for this dilution effect - which scales with $1/(1+\Delta)$, the factor approaches 4.78
474 per meg ppm⁻¹. The scaling of dilution effects is independent on which air component is
475 changing and it affects all air components relative to their molecular fractions similarly. O₂

476 values on a CRDS or paramagnetic cell instrument is affected even if there is no change in O₂
477 or N₂ but only in CO₂ or water vapor or any other component which is present. This is in
478 contrast to measurements of O₂/N₂ ratios for the same case where equal ratio would be
479 measured. Major dilution influences are expected from O₂, CO₂ and H₂O changes due to
480 natural exchange processes on air samples or when using artificial air-like compositions.

481 3.2.2. Measurements of ambient air

482 Ambient air measurements were conducted from the roof top of our laboratory at the
483 University of Bern to evaluate the analyzer's performance under atmospheric variability.
484 Ambient air was continuously aspirated from the inlet at the roof of the building at a flow rate
485 of ~ 250 sccm which is then dried using a cooling trap kept at -90 °C towards the switching
486 valve (V1) and measured in similar way to the standard gases as explained above. The
487 measurement values obtained here were compared with the parallel measurements by the
488 Paramagnetic sensor to test the instruments stability and accuracy.

489 Figures 13 panels a & b show the 1-minute average ambient air measurements from the
490 rooftop inlet by the Paramagnetic and the CRDS analyzers at the beginning of the testing
491 period including standard gases measured every 12-hour. While the Paramagnetic analyzer
492 seems to be stable, the CRDS analyzer showed a strong drift for an extended period. This can
493 be due to unstable conditions in the CRDS measurement system as it started operating right
494 after it was unpacked. Hence, we looked into temperature inside the instrument chassis and
495 pressure records, which were stable within the manufacturer's recommended range during this
496 period. As the CRDS analyzer incorporates a water correction function, interference from this
497 species should be well accounted. Even comparing the analyzer's parallel water
498 measurements to water measurements by the NDIR system such a drift was not observed. It
499 should be noted that the two internal standard gases which were less frequently measured

500 (every 12 hours) during this period were also drifting following similar pattern. This implies
501 that the drift is associated with the analyzer. Interestingly, this pattern can be modeled using a
502 polynomial function which can then be used to correct for the observed drift in the ambient air
503 measurements. After applying a polynomial drift correction, we were able to fully accounted
504 for the observed drift. However, the manufacturer decided to further investigate possible
505 causes of this drift. After further improvements, we obtained the first commercial analyzer in
506 September 2017 and repeated the above tests (Figure 13 c & d). No such drift was observed
507 any more in the standard gases or in ambient air measurements.

508 We believe that the optical amplifier has caused the drift in the first system and not anymore
509 included in the design of the product which produced a significant amount of broadband light
510 that could fill the cavity (albeit with a low coupling coefficient), and would ring down with a
511 different (and generally much faster) time constant than the baseline loss of the cavity.
512 However, the ringdown time on the peak of the oxygen line is just 10 microseconds, such that
513 the broadband light might have distorted the single exponential decay of the central laser
514 frequency, leading to the observed drift in the oxygen signal. However, we were not able to
515 confirm this hypothesis.

516 3.2.3. Water correction test

517 Measurements of oxygen are reported as both wet ($O_{2, raw}$) and dry ($O_{2, dry}$) mole
518 fractions by the CRDS analyzer as it also measures water vapor in parallel at its water
519 absorption line (7817 cm^{-1}), and corrects for the dilution effect based on an inbuilt numerical
520 function:

$$521 \quad O_{2,dry} = \frac{O_{2,raw}}{1-H_2O} \quad (5)$$

522 where H_2O is the measured water mole fraction.

523 The efficiency of water correction by this function was assessed in two ways: i) by comparing
524 the water vapor content in standard air measured by this analyzer with similar measurements
525 by the NDIR analyzer and ii) by comparing the oxygen mixing ratios between non-dried
526 ambient air measured and corrected for water dilution by the CRDS analyzer with dried air
527 measured using a paramagnetic analyzer.

528 Figure 14 shows the water vapor content for standard gases measured continuously for
529 two days by the CRDS and the NDIR analyzers. Note that the two data sets are manually
530 fitted to each other as the measured water values by the NDIR analyzer are not calibrated.
531 Based on this plot, the two analyzers are in very good agreement although there are small
532 differences during very dry conditions (low water content).

533 Figure 15a shows the dried ambient air water measurements in both analyzers with
534 frequent spikes due to valve switching while measuring standard gases. In the second case,
535 where the water trap was by-passed and non-dried air was allowed to the CRDS analyzer
536 keeping the dried air flow to the NDIR (Figure 15b), a clear increase in the water
537 measurements in the CRDS analyzer can be observed. Here, it should be noted that there are
538 no spikes in the water measurements of the CRDS analyzers as there are no standard gas
539 measurements in between and the inlet is directly connected to the CRDS analyzer (Figure
540 11). Figures 15c & 15d show the difference in oxygen measurements of ambient air measured
541 in both analyzers in the two cases stated above (note that the CRDS uses its built-in water
542 correction function applying Eq. 5). The measurements of the Paramagnetic analyzer were
543 scaled to ppm units by applying the correlation equation obtained from the six standard gas
544 measurements of the two analyzers (Fig. A.1). Note that the CRDS measurements were
545 corrected for the observed drift using the polynomial fit to the two standard gas measurements
546 stated above.

547 In the first period of the measurement when both analyzers measured dried ambient
548 air, the absolute differences between the 1-minute averages measured over two days by the
549 two analyzers were mostly within 15 ppm (Figure 15c) and symmetrically distributed around
550 zero (Figure 15e). However, when wet air was admitted to the CRDS analyzer and the in-built
551 water correction was applied, a stronger variability was observed in the calculated differences
552 (Figure 15d). This implies stronger short term variability in the CRDS analyzer measurement
553 values (as nothing was changed for the Paramagnetic measurement system) when wet samples
554 were analyzed. The more negative values in the differences (Figure 15f) can also be
555 associated with overestimation of the O₂ mixing ratios by the CRDS originating from an
556 overestimated water correction. However, detailed evaluation of the analyzer's water
557 correction function is beyond the scope of this study.

558 **3.3. Field Measurements**

559 After a series of tests at University of Bern, we conducted multiple field measurements
560 at the High Altitude Research Station Jungfrauoch and the Beromünster tall tower sites in
561 Switzerland described below.

562 **3.3.1. Tests at the High Altitude Research station Jungfrauoch**

563 The High Alpine research station Jungfrauoch is located on the northern ridge of the
564 Swiss Alps (46° 33' N, 7° 59' E) at an elevation of 3580 m a.s.l. It is one of the global
565 atmospheric watch (GAW) stations well-equipped for measurements of numerous species and
566 aerosols. The site is above the planetary boundary layer most of the time due to its high
567 elevation (Henne et al., 2010; Zellweger et al., 2003). However, thermally uplifted air from
568 the surrounding valleys during hot summer days or polluted air from the heavily industrialized
569 northern Italy may reach at this site (Zellweger et al., 2003). The Division of Climate and
570 Environmental Physics at the University of Bern has been monitoring CO₂ and O₂ mixing

571 ratios at this site based on weekly flask sampling and continuous measurements since 2000
572 and 2004, respectively (Schibig et al., 2015). The CO₂ mixing ratio is measured using a
573 commercial NDIR analyzer (S710 UNOR, SICK MAIHAK) while O₂ is measured using the
574 Paramagnetic sensor (PM1155 oxygen transducer, Servomex Ltd, UK) and fuel cells (Max-
575 250, Maxtec, USA) installed inside a home-built controlling unit. Similar to the comparison
576 tests at the University of Bern, we have conducted parallel measurements between the CRDS
577 analyzer and the paramagnetic cell at this high altitude site during 03 – 14 February 2017. The
578 measurement of ambient air at the Jungfrauoch system is composed of sequential switching
579 between low span (LS) and high span (HS) calibration gases followed by a target gas (T)
580 measurement (once a day) to evaluate the overall system performance and finally a working
581 gas (WG) measurement before switching back to ambient air.

582 Figure 16 (top panel) shows the calibrated 1-minute averaged O₂ mixing ratios
583 measured at this high altitude site in comparison with the Paramagnetic oxygen analyzer
584 already available at the site. Despite the strong variability observed during the measurement
585 period of 10-days by both analyzers, a very good agreement was observed between them.

586 Figure 16 (bottom panel) shows the absolute difference of 1-minute averages in
587 atmospheric O₂ measured at Jungfrauoch between the two analyzers which are mostly within
588 ± 5 ppm range (but sometimes going as high as ± 10 ppm) without an offset. However, for
589 generally reported 10-minutes, half-hourly or hourly means these values correspond to < 1.5
590 ppm, < 1 ppm and < 0.65 ppm.

591 3.3.2. Tests at the Beromünster tall tower site

592 The Beromünster tower is located near the southern border of the Swiss Plateau, the
593 comparatively flat part of Switzerland between the Alps in the south and the Jura mountains
594 in the northwest (47° 11' 23" N, 8° 10' 32" E, 797 m a.s.l.), which is characterized by intense

595 agriculture and rather high population density. A detailed description of the tower
596 measurement system as well as a characterization of the site with respect to local
597 meteorological conditions, seasonal and diurnal variations of greenhouse gases, and regional
598 representativeness can be obtained from previous publications (Berhanu et al., 2016; Berhanu
599 et al., 2017; Oney et al., 2015; Satar et al., 2016). The tower is 217.5 m tall with access to five
600 sampling heights (12.5 m, 44.6 m, 71.5 m, 131.6 m, 212.5 m) for measuring CO, CO₂, CH₄
601 and H₂O using Cavity Ring Down Spectroscopy (Picarro Inc., G-2401). By sequentially
602 switching from the highest to the lowest level, mixing ratios of these trace gases were
603 recorded continuously for three minutes per height, but only the last 60 seconds were retained
604 for data analysis. The calibration procedure for ambient air includes measurements of
605 reference gases with high and low mixing ratios traceable to international standards (WMO-
606 X2007 for CO₂ and WMO-X2004 for CO and CH₄), as well as target gas and more frequent
607 working gas determinations to ensure the quality of the measurement system. From two years
608 of data a long-term reproducibility of 2.79 ppb, 0.05 ppm, and 0.29 ppb for CO, CO₂ and
609 CH₄, respectively was determined for this system (Berhanu et al., 2016).

610 Between 15.02.2017 and 02.03.2017, we have connected the new CRDS oxygen
611 analyzer in series with the CO₂ analyzer (Picarro G-2401) and measured the O₂ mixing ratios
612 at the corresponding heights. Similar to the CO₂ measurements, O₂ was also measured for
613 three minutes at each height. During this period, we have evaluated the two features (isotopic
614 mode and concentration mode) of the CRDS analyzer. In the isotopic mode, the CRDS
615 measures the $\delta^{18}\text{O}$ values as well as the O₂ concentration while in concentration mode only
616 the latter was measured.

617 During the tests conducted at this tower site, we first evaluated the two operational
618 modes (concentration vs isotopic modes) of the CRDS analyzer. Ambient air measurements

619 on isotopic mode over a 4-days period showed a strong variability in the measured oxygen
620 mixing ratios and it was not possible to distinguish the variability in the O₂ mixing ratios
621 among the five height levels. The calculated 1-minute standard error for ambient air
622 measurements was as high as 10 ppm while a standard error of less than 1 ppm was
623 determined from similar measurements in the concentration mode. Additionally, comparing
624 the O₂ values between the two modes, frequent short time variation in ambient air O₂ (~ 200
625 ppm) was observed in the isotope mode measurements while the variation in the concentration
626 mode is significantly smaller (~ 30 ppm). This precision degradation is due to the weaker ¹⁶O
627 oxygen line used for the isotopic mode, and the fact that far more ring-downs are collected on
628 the rare isotopologue in isotopic mode. Hence, we have conducted the remaining test
629 measurements in concentration mode.

630 As this tower has five sampling height levels, we first followed three minutes of
631 switching per inlet level, which enables four measurements per hour at a given level.
632 However, we noticed hardly any difference among the different levels due to strong short
633 term variability in O₂ mixing ratios between the consecutive heights. Hence, we switched to a
634 longer sampling period of six-minutes per height. Figure 17 shows the diurnal CO₂ and O₂
635 variations at the lowest (12 m) and highest (212.5 m) sampling heights of the tower. These
636 two heights were selected simply to better illustrate the difference in the mixing ratios. The
637 CO₂ mixing ratios on the top panel show higher values at the 12 m inlet than the highest level
638 most of the day due to its closeness to sources except during the afternoon (11:00 - 17:00
639 UTC) when both levels show similar but decreasing CO₂ mixing ratios. This is due to
640 presence of a well-mixed planetary boundary layer (PBL) (Satar et al., 2016). The lag in CO₂
641 peak between the two height levels by about two hours indicates the duration for uniform
642 vertical mixing along the tower during winter 2017. The opposite variability patterns are also

643 clearly visible in the O₂ mixing ratios shown in the lower panel with a clear distinction
644 between the two height levels during early in the morning and in the evening while similar O₂
645 values were observed in the afternoon. These opposing profiles are expected as CO₂ and O₂
646 are linearly coupled with a mean oxidation ratio of -1.1 ± 0.05 (Severinghaus, 1995) for land-
647 biospheric processes (photosynthesis and respiration) and -1.44 ± 0.03 for fossil fuel burning
648 (Keeling, 1988b).

649 Table 2 shows the oxidation ratios derived as the slopes of the linear regression
650 between CO₂ and O₂ mixing ratios at the different height levels measured on 25 February
651 2017. Accordingly, height dependent slopes were observed with a slope of -0.98 ± 0.06 at the
652 lowest level, close to the biological processes induced slope but slightly lower than its mean
653 value. For the highest level, we calculated a slope of -1.60 ± 0.07 a value close to fossil fuel
654 combustion oxidation ratio. Note that depending on fossil fuel type the oxidation ratio can
655 range between -1.17 and -1.95 for coal and natural gas, respectively (Keeling, 1988b). While
656 the slopes derived for the two other levels (44.6 m and 131.6 m) show similar values between
657 the highest and lowest height levels, possibly from mixed sources, the middle level showed a
658 slightly higher slope than these two levels but still in the large range between the lowest and
659 highest inlet heights.

660 3.4. Evaluation of the $\delta^{18}\text{O}$ measurements

661 To further evaluate the analyzer's performance in measuring stable oxygen isotopes,
662 we conducted ambient air isotopic composition measurements as well as analyzed a standard
663 gas without CO₂ which has a known $\delta^{18}\text{O}$ value. The choice of this CO₂-free air standard gas
664 is twofold: one it has a known $\delta^{18}\text{O}$ value and second as it has no interference from possible
665 CO₂ absorption band overlap. For this test three 0.5 L glass flasks were preconditioned and
666 filled with this standard gas to ambient pressure. These flasks were attached before or after

667 the water trap (Fig. 11) and measured similar to ambient air measurements. These
668 measurements were then compared with $\delta(^{34}\text{O}/^{32}\text{O})$ values obtained by parallel measurements
669 using our IRMS.

670 Figure 18 shows the $\delta^{18}\text{O}$ values of ambient air from the roof top with three
671 consecutive measurements of glass flasks filled with CO_2 -free air in-between followed by a
672 fourth flask filled with breath air. An excellent agreement was observed for measurements
673 from both instruments for the three flasks filled with a standard gas. However, the fourth flask
674 with breath air showed a signal opposite to the measurements by the IRMS. As breath air
675 contains large amount of water and CO_2 in addition to O_2 , which can possibly interfere with
676 the CRDS analyzer measurements, we have removed H_2O and CO_2 by using a cryogenic trap
677 ($-130\text{ }^\circ\text{C}$) and in an additional experiment using Schütze reagent to remove both CO and CO_2 .
678 However, we have not observed any improvement towards an agreement with the IRMS
679 measurements. Therefore, any other gas component in the breath air must be relevant for the
680 interference. Based on the absorption lines in the spectral range of the instrument (7878 cm^{-1})
681 retrieved from HITRAN database, we expect interference either from carbon monoxide (now
682 excluded by the tests) or methane or VOCs including acetone, ethanol, methanol or isoprenes,
683 all of which have been measured in breath air (Gao et al., 2017; Gottlieb et al., 2017; McKay
684 et al., 1985; Ryter and Choi, 2013; Wolf et al., 2017). Further investigations have to shed light
685 on these interferences in order to take corresponding action to surpass these shortcomings in
686 the isotope analysis based on cavity ring-down spectroscopy.

687 **4. Conclusions**

688 We have thoroughly evaluated the performance of a new CRDS analyzer which
689 measures O_2 mixing ratios and isotopic composition combining laboratory and field tests.
690 Even if a drift in the analyzer was observed at the beginning of this study, which can be easily

691 corrected by calibration, the recent analyzers built by the manufacturer did not show such
692 instrumental drift. However, prior tests are recommended to see the analyzer's stability.

693 The T-split tests for the current measurement setup based on the measurements of two
694 standard gases showed a difference within the measurement uncertainty. However, this effect
695 may become significant while applying larger splitting ratios and we recommend conducting
696 further experiments to accurately quantify this influence for larger splitting ratios.

697 We have observed a strong influence of dilution in the measured O₂ values during the
698 presence of high CO₂ mixing ratios. Even if such an influence may not be critical for the
699 present study, such an effect might be significant in other studies where higher CO₂ mixing
700 ratios might be present and we recommend following a correction strategy based on parallel
701 CO₂ measurements. This also applies for more accurate analysis.

702 The water correction applied by the instrument's in-built function seems to sufficiently
703 correct for the water vapor influence. However, a larger variability of the difference was
704 observed between the CRDS analyzer and the Paramagnetic cell when dried samples were
705 used in both systems. This can possibly be due to an overcorrection by the water correction
706 function of the CRDS analyzer when dried samples were used. This is particularly true for the
707 very low water vapor range (< 100 ppm). We believe that it is important to further investigate
708 this issue and identify an improved water correction strategy.

709 Based on the analysis of O₂ mixing ratios in the concentration and isotopic modes, we
710 have observed a significant decrease in precision (about ten-fold) in the latter measurement
711 mode. The measured $\delta^{18}\text{O}$ values for the standard air by the CRDS analyzer are in excellent
712 agreement with the IRMS values. However, such measurements for a breath air showed a
713 contrasting signal, possibly due to interference from other gases such as CH₄. Hence, we
714 recommend further investigation on such possible contaminants and how to possibly remove

715 them while conducting ambient air measurements. However, we believe that this analyzer can
716 be used for tracer experiments where artificially enriched isotopes are used to study biological
717 processes such as photosynthesis in plants using isotopically labelled CO₂ and H₂O.

718 **Acknowledgement**

719 We would like to thank ICOS-RI and the Swiss National Science Foundation (SNF) for
720 funding ICOS-CH (20FI21_148994, 20FI21_148992). We are also grateful to the
721 International Foundation High Alpine Research Stations Jungfrauoch and Gornergrat. The
722 measurement system at the Beromünster tower was built and maintained by the CarboCount-
723 CH (CRSII2_136273) and IsoCEP (200020_172550) projects both funded by SNF.

724

725

726

727

728

729

730

731

732

733

734

735

736

737

738

739 List of Tables

740 Table 1. Assigned mixing ratios of standard gases used in this study and their corresponding
 741 values measured by the NDIR, CRDS and IRMS at the University of Bern. ¹The assigned
 742 values are based on measurements from different institutions (University of Bern (UB),
 743 Scripps or NOAA, see column cylinder name). ²Measurements are on the Bern scale for CO₂
 744 and O₂. The Bern scale is shifted by +550 per meg. ³Values on the Scripps scale.

745

Cylinder name	Assigned CO ₂ (ppm) ¹	Assigned O ₂ (per meg) ¹	CO ₂ -IRMS (ppm) ²	CO ₂ -NDIR (ppm) ²	O ₂ -IRMS (per meg) ²	O ₂ -Paramagnetic (per meg) ²	O ₂ -CRDS (per meg) ²
ST-1 LUX3576- UB	427.47	-1026	427.47	427.59	-1026	-1070	-1057
ST-2 LK922131- UB	368.09	599	368.09	367.82	599	560	590
ST-3 CA07045- Scripps	382.303	-271.6	382.50	381.99	278 (-272.2) ³	302	281
ST-4 CA07043- Scripps	390.528	-476.4	390.69	390.15	71 (-479.5) ³	66	63
ST-5 CA07047- Scripps	374.480	-807.7	374.70	374.17	-253 (-803.3) ³	-212	-233
ST-6 CA04556- NOAA	192.44	-3410	191.21	191.64	-3410	-2905	-3013
ST-7 CA06943-	2699.45	-		2612.80	-	-2691	-3369

NOAA							
ST-8 LK76852- UB	411.49	37794	411.49	406.25	37794	34513	36017

746

747

748 Table 2. The CO₂ and O₂ correlation coefficients at the different height levels derived using
749 the least square fit and the correlation coefficients (r^2). Uncertainties are calculated as
750 standard error of the slope.

Height	Oxidation Ratios (O ₂ :CO ₂)
12.5 m	-0.98 ± 0.06 (0.48)
44.6 m	-1.29 ± 0.07 (0.50)
71.5 m	-1.49 ± 0.08 (0.47)
131.6 m	-1.23 ± 0.05 (0.55)
212.5 m	-1.60 ± 0.07 (0.61)

751

752

753

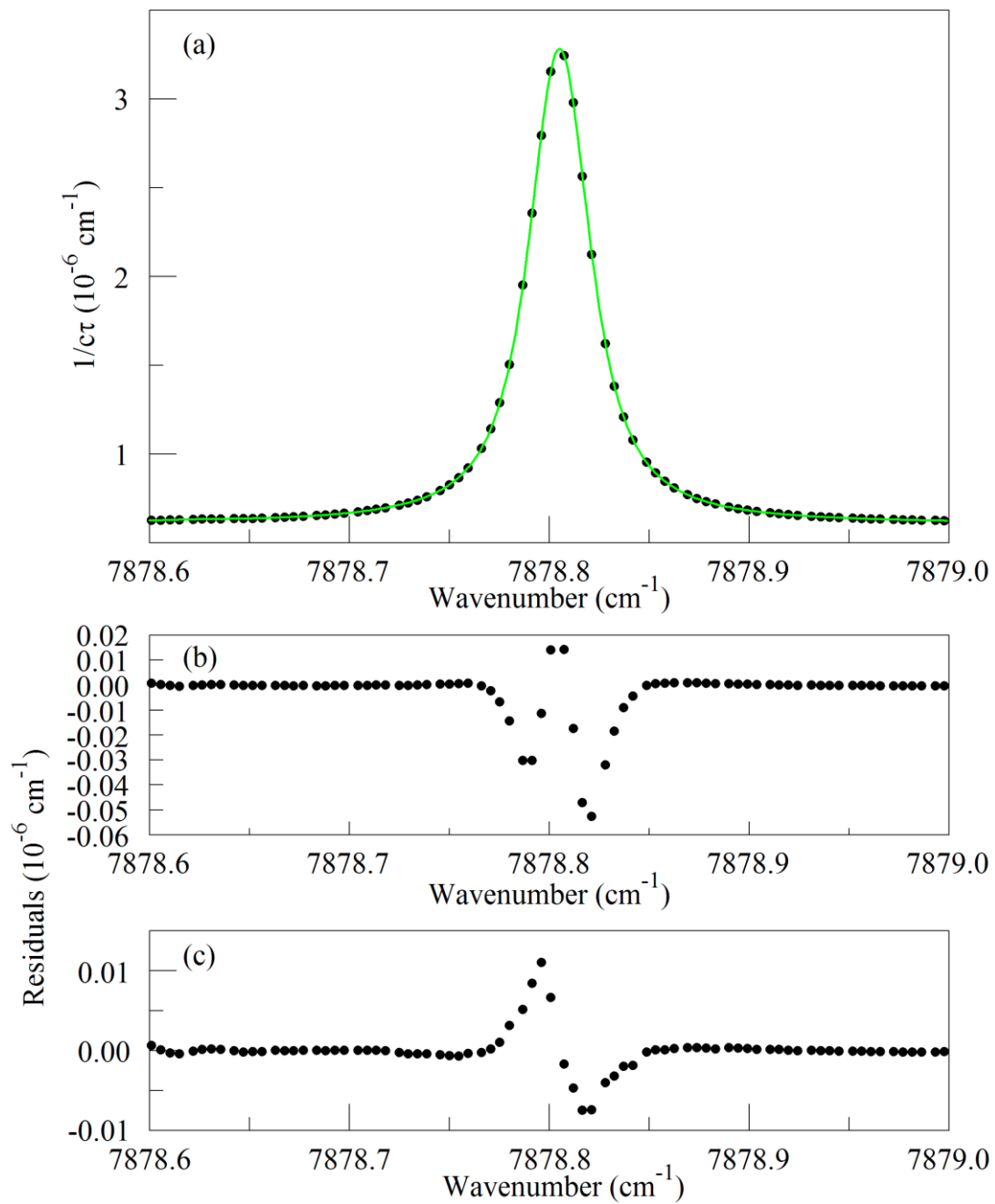
754

755

756

757

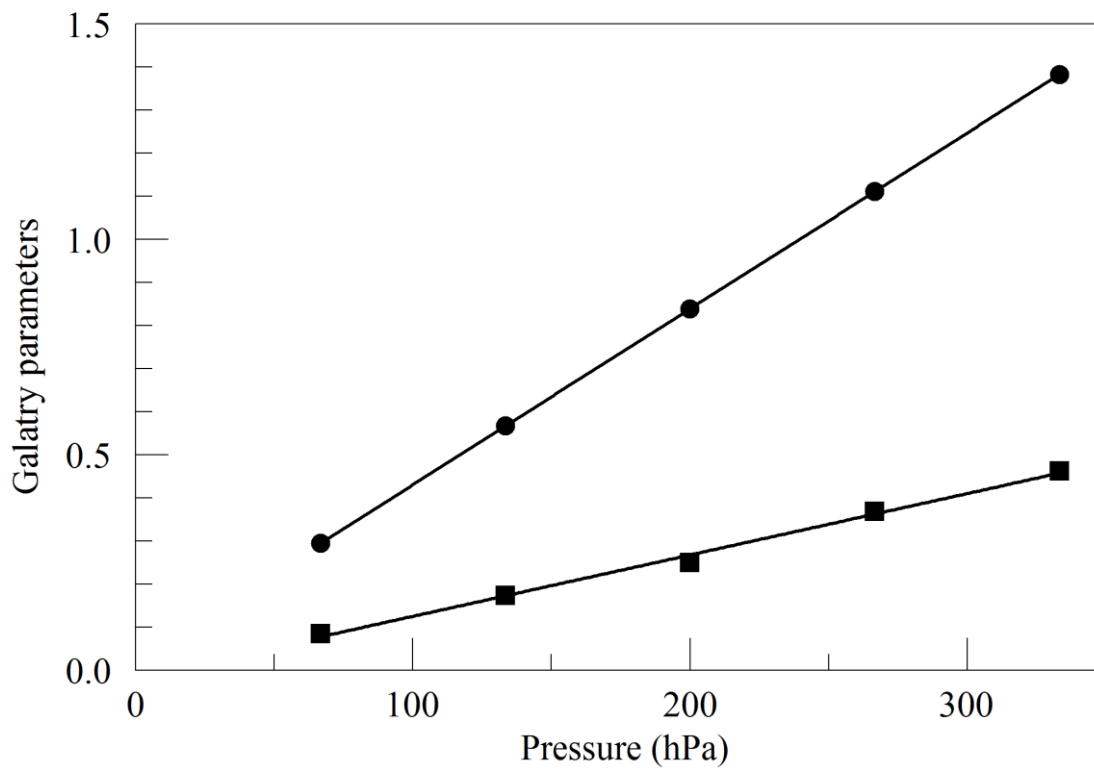
758



760

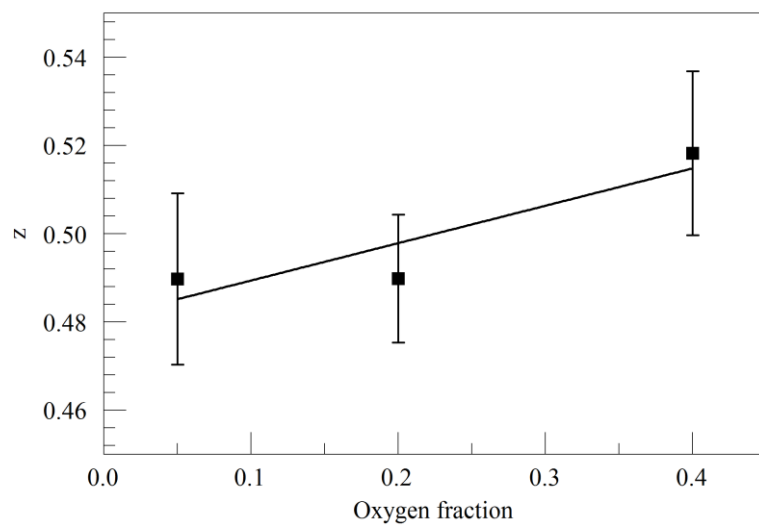
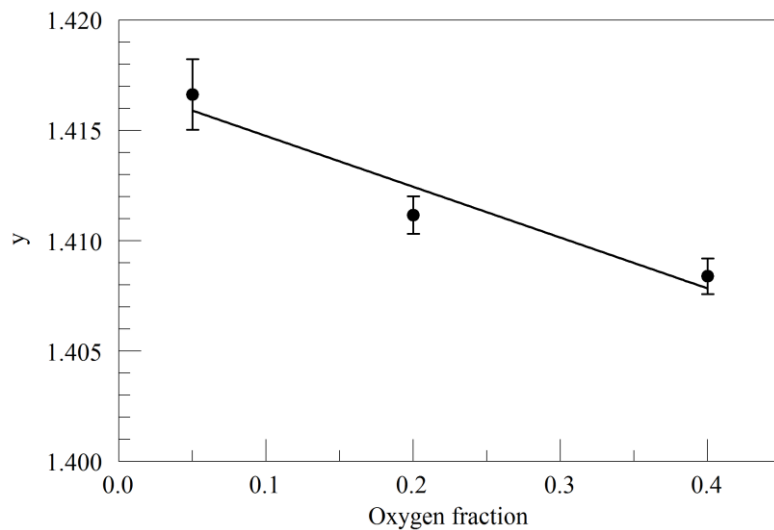
761 Figure 1. The top panel (a) shows the raw data (points) and the best-fit Galatry function (solid
 762 line). Residuals of the Voigt fit are shown in panel (b) and residuals of the Galatry fit are
 763 shown in panel (c).

764



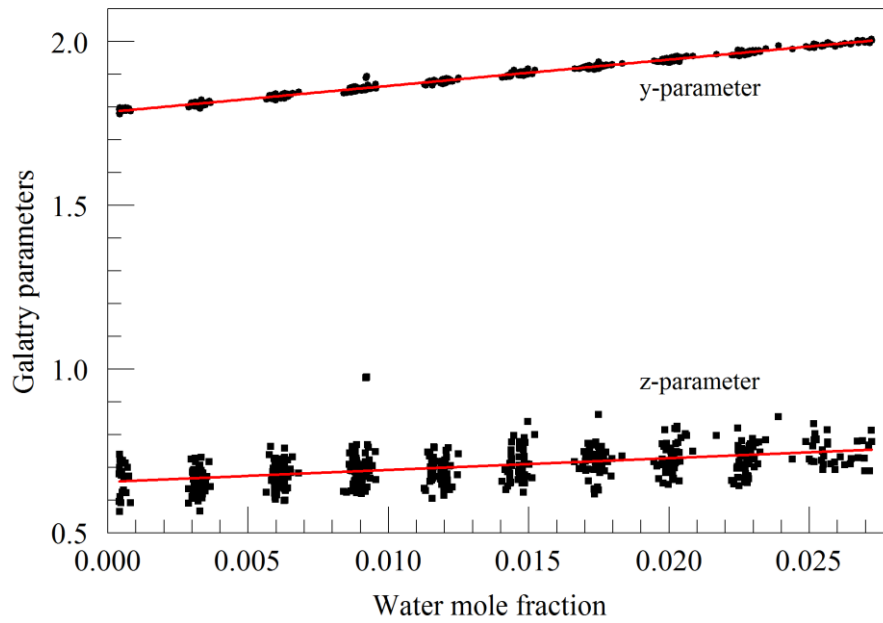
766

767 Figure 2. Best-fit values for the Galatry parameters of the Q13Q13 line of O₂, as a function of
 768 pressure. The line broadening parameter y is represented by circles and the line narrowing
 769 parameter z by squares. The solid lines are linear fits to the measurements. The best-fit offset
 770 and slope are 0.0227 and $0.004082 \text{ hPa}^{-1}$ for y , and -0.0169 and $0.001424 \text{ hPa}^{-1}$ for z .



771

772 Figure 3. Galatry parameters of the Q13Q13 line of O₂ at 340 hPa and 45° C as a function of
 773 O₂ mole fraction in binary O₂ - N₂ mixtures. The linear fits to the data are $y = 1.417 - 0.023 x$
 774 f_{O_2} and $z = 0.481 + 0.085 x f_{O_2}$.



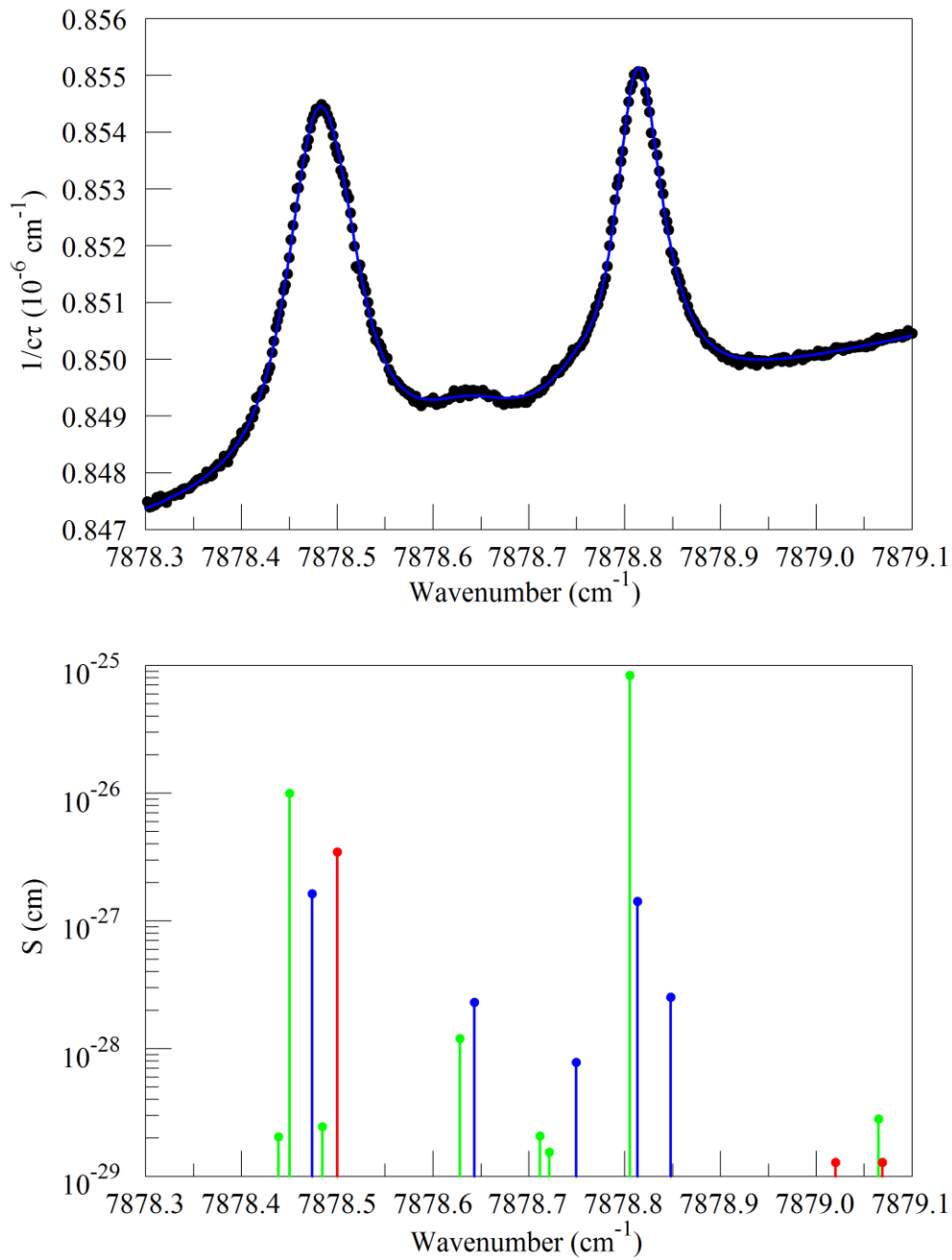
775

776 Figure 4. Galatry parameters of the $7816.75210 \text{ cm}^{-1}$ water line in air at 340 hPa and 45° C as
 777 a function of water mole fraction. Black points are from measurements and red lines are
 778 linear fits: $y = 1.7846 + 8.01 \times f_{\text{H}_2\text{O}}$ and $z = 0.656 + 3.60 \times f_{\text{H}_2\text{O}}$.

779

780

781



782

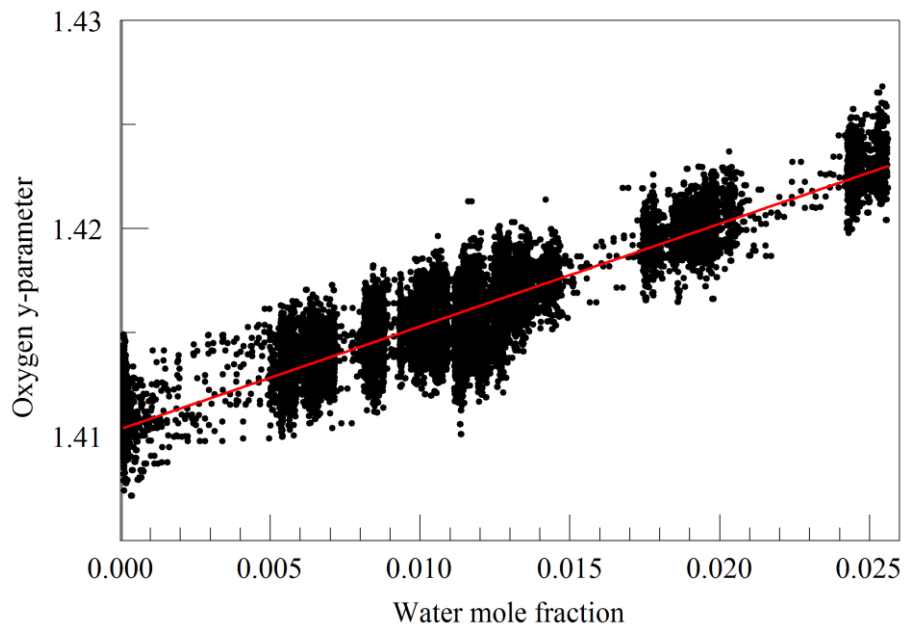
783 Figure 5. Upper panel: spectrum of water in nitrogen (points) and fit to Voigt model (blue

784 curve). Lower panel: Oxygen (green), normal water (blue), and deuterated water (red) lines

785 in the 2016 Hitran data base.

786

787



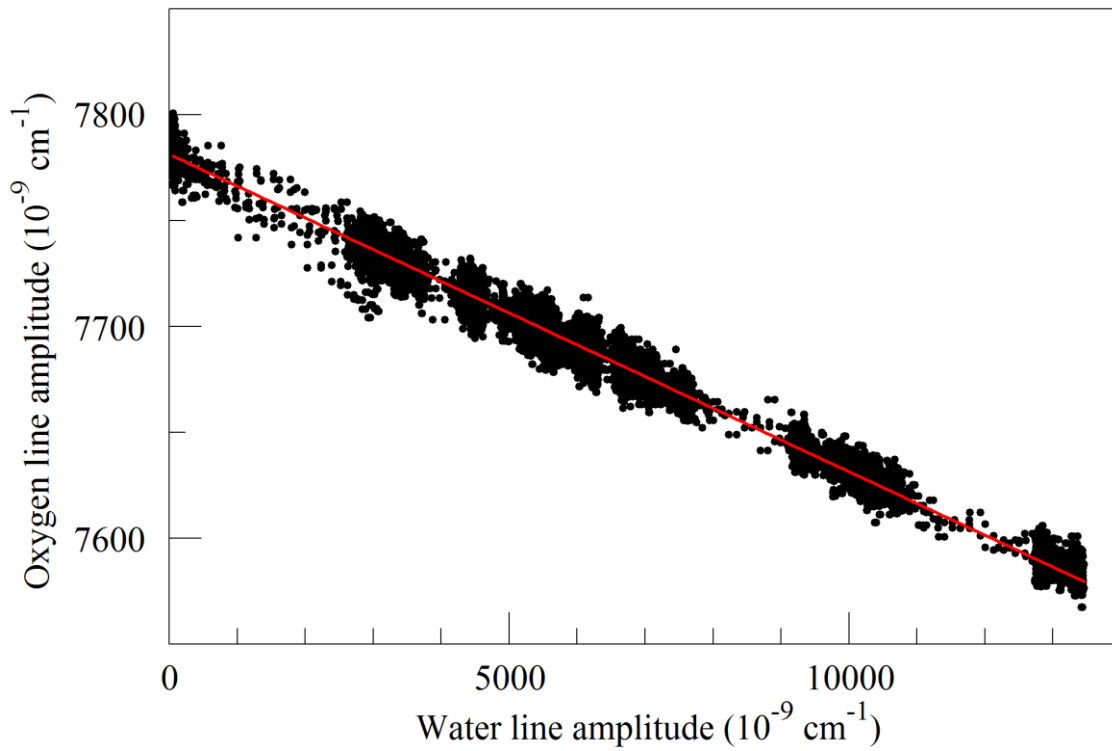
788

789 Figure 6. Galatry collisional broadening parameter of the oxygen Q13Q13 line at 340 hPa
790 and 45° C versus water mole fraction. Black points are from measurements and the red line is
791 a linear fit: $y = 1.4109 + 0.467 f_{\text{H}_2\text{O}}$.

792

793

794



795

796 Figure 7. Measured absorption line amplitudes for oxygen and water vapor for water vapor
 797 mixing ratios ranging from nearly 0 to 0.025. Black points are from measurements and the
 798 red line is a linear fit: with intercept $7.78001 \times 10^{-6} \text{ cm}^{-1}$ and slope -0.014807 .

799

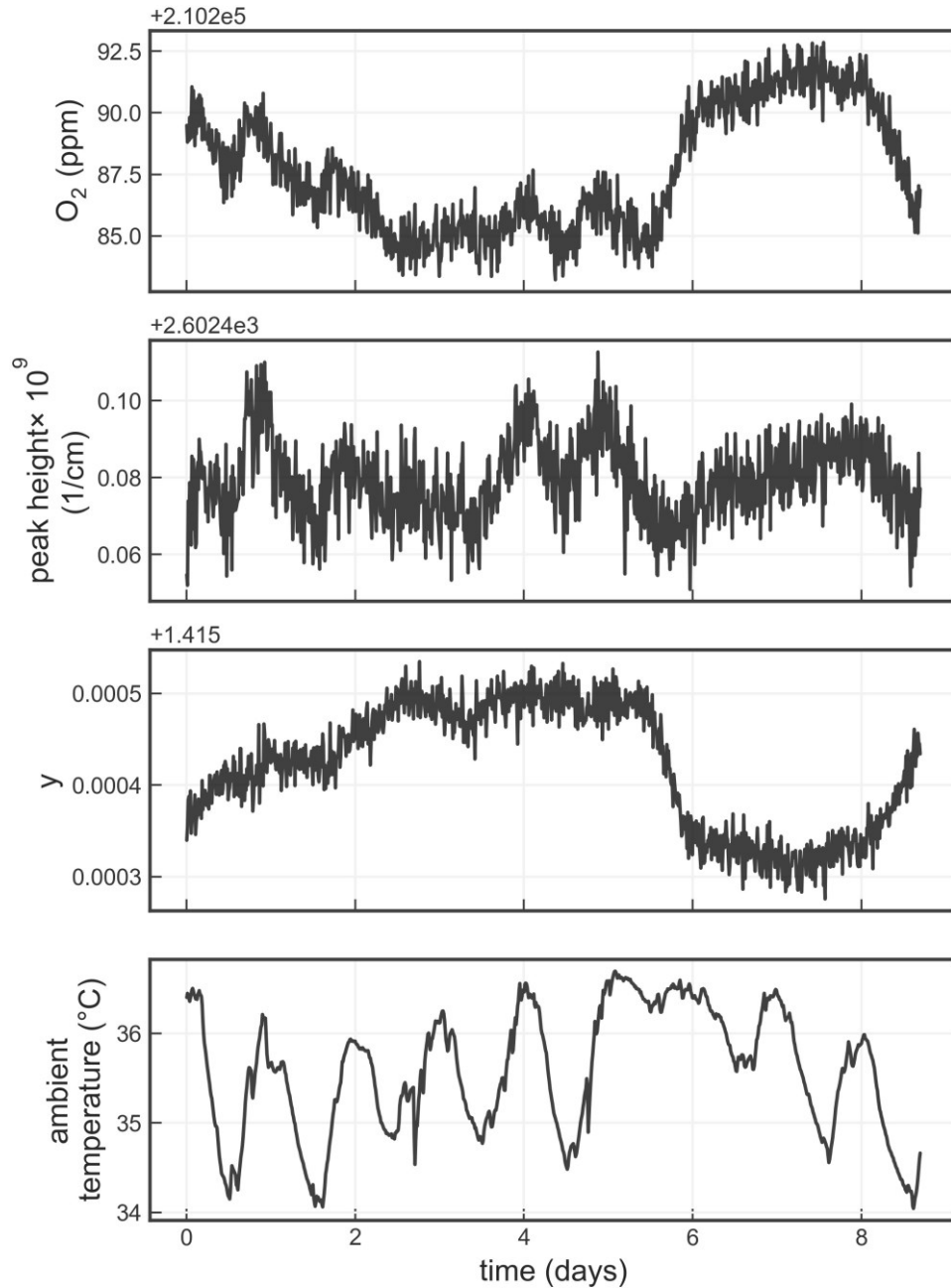
800

801

802

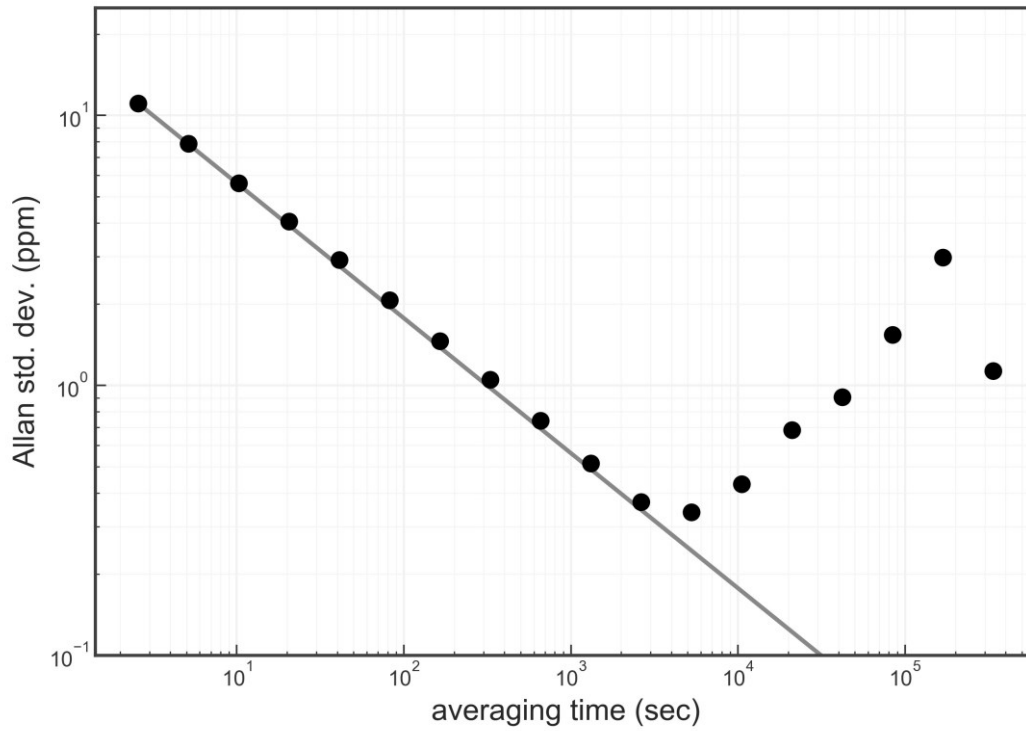
803

804



805

806 Figure 8. Time series from a measurement of a single tank over about a week. The four panels
 807 show the water-corrected oxygen concentration, the absorption peak loss minus the baseline
 808 loss, the measured Lorentzian broadening factor, and the ambient temperature (measured in
 809 the instrument housing), respectively. A windowed average of 300 seconds was applied to all
 810 four data sets.



811

812 Figure 9. Precision of O₂ mole fraction measured from a tank of synthetic air. Filled circles

813 are measurements and the line shows the ideal $\tau^{-1/2}$ dependence.

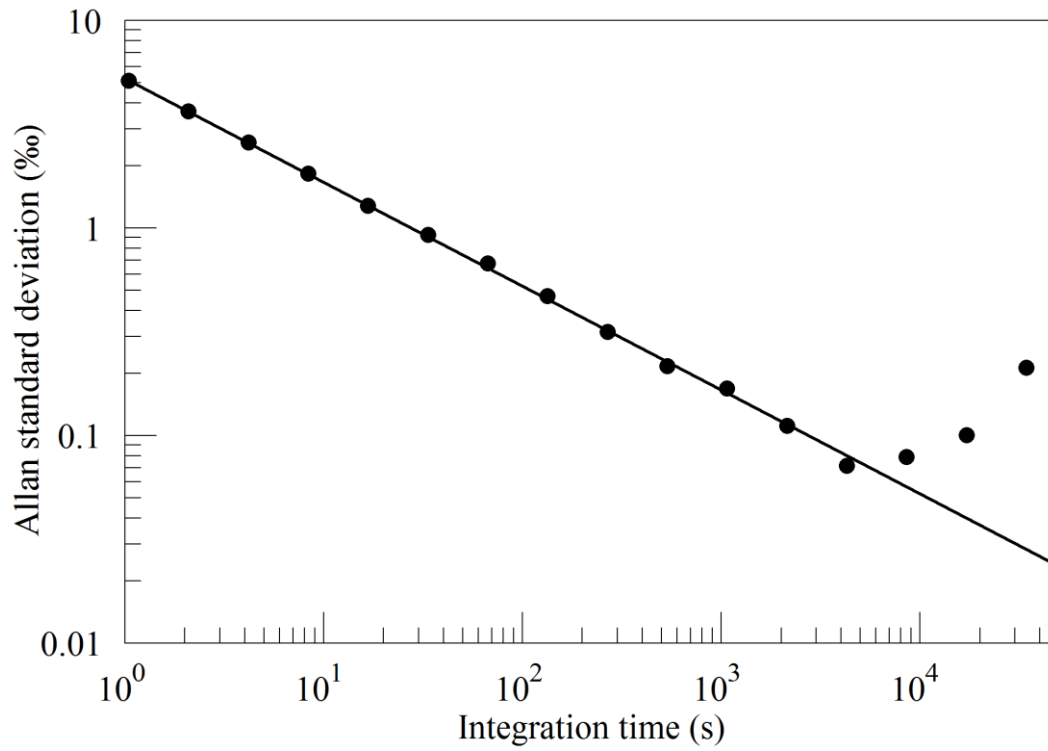
814

815

816

817

818



819

820 Figure 10. Precision of $\delta(^{18}\text{O})$ measured from a tank of synthetic air. Filled circles are

821 measurements and the line shows the ideal $\tau^{-1/2}$ dependence.

822

823

824

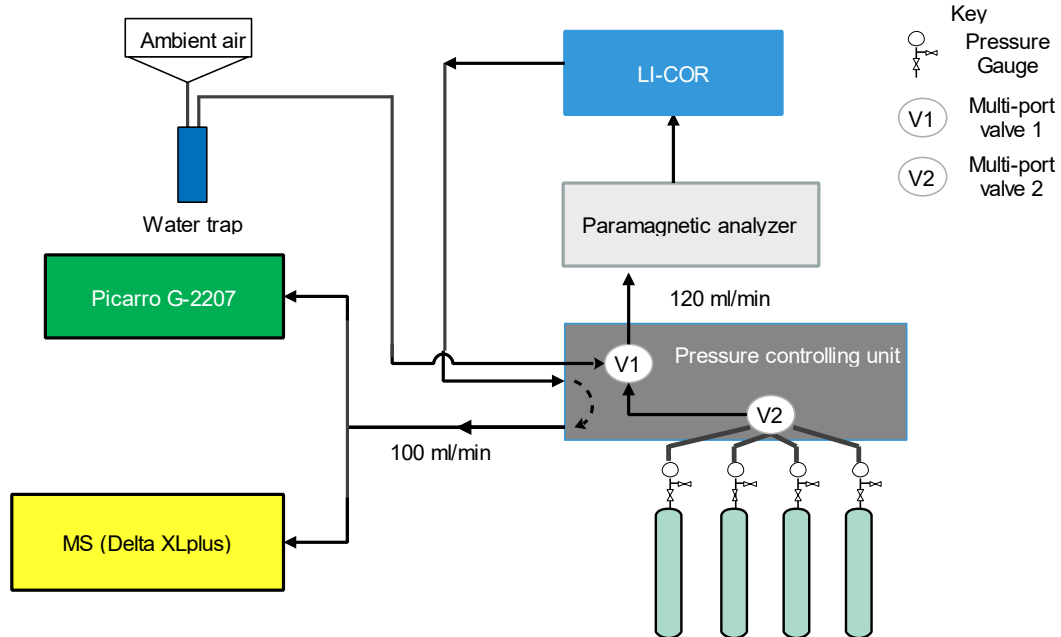
825

826

827

828

829



830

831 Figure 11. Schematics of the measurement system used to compare the Picarro analyzer with
 832 the Mass Spectrometer at Bern.

833

834

835

836

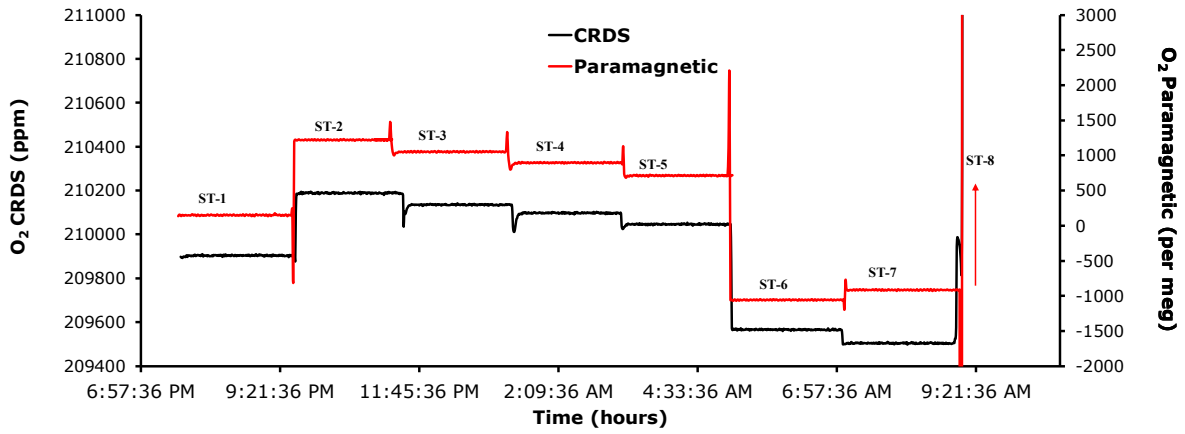
837

838

839

840

841



842

843 Figure 12. Comparison of oxygen mixing ratios for the seven standard gases measured using
 844 the CRDS analyzer (black) and the Paramagnetic sensors (red).

845

846

847

848

849

850

851

852

853

854

855

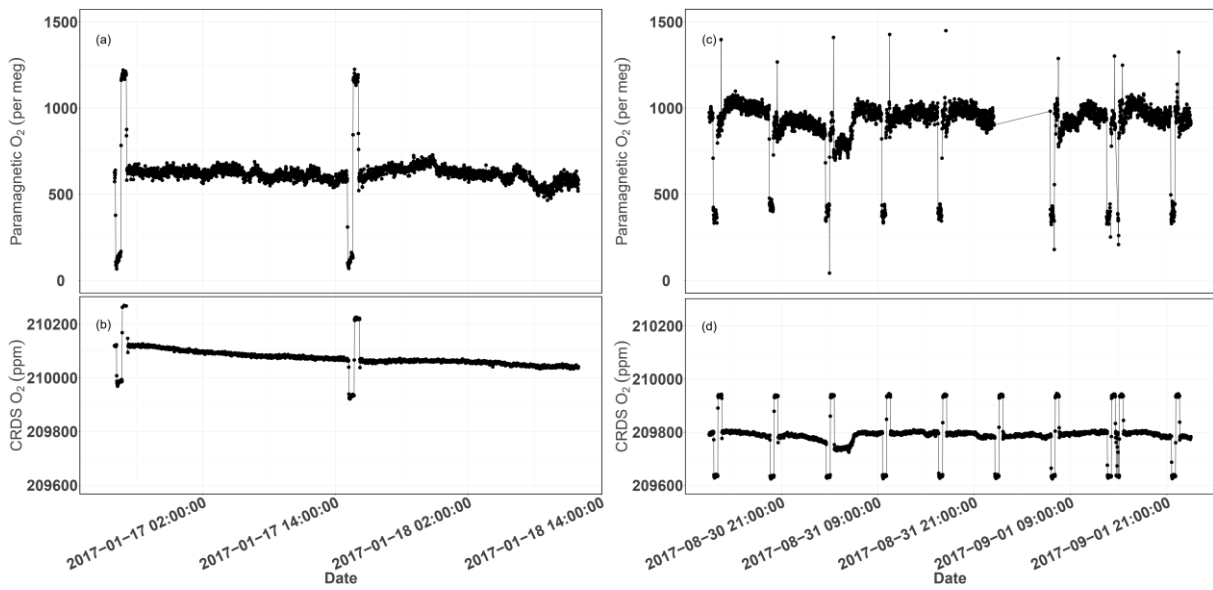
856

857

858

859

860



861

862 Figure 13. Parallel ambient air measurements by the Paramagnetic and CRDS analyzers at the
863 beginning of the testing period (Panels a & b, January 2017) and the second phase of testing
864 (Panels c & d, September 2017). The spikes are measurements from the two standard gases
865 bracketing the ambient air values.

866

867

868

869

870

871

872

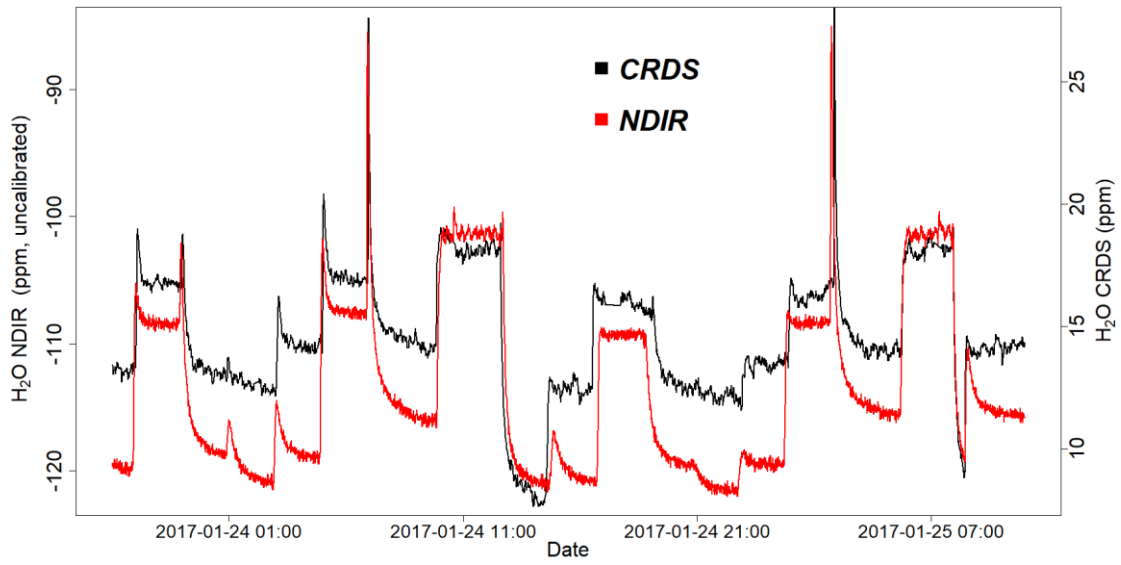
873

874

875

876

877



878

879 Figure 14. Parallel water vapor measurements for a dried ambient air by both the NDIR and
880 CRDS analyzers. Note that the water values from the NDIR analyzer are not calibrated.

881

882

883

884

885

886

887

888

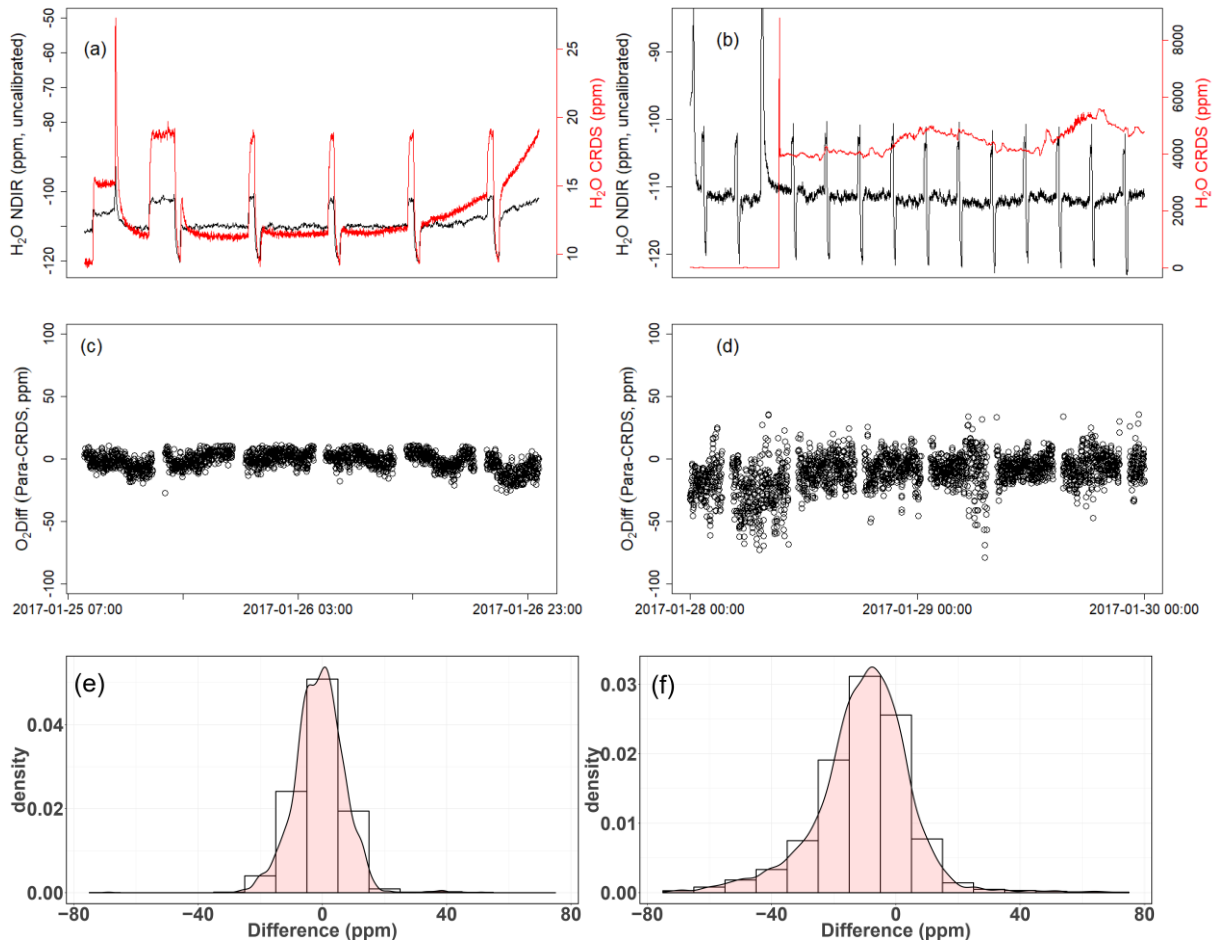
889

890

891

892

893



894

895

896 Figure 15. Results of water correction tests. Water measurements of the NDIR (left scale) for
897 dry conditions (a,b) and the CRDS analyzer (right scale) for dry (a) and wet (b) conditions.
898 The difference in oxygen measurements between the Paramagnetic and the CRDS instrument
899 using the built-in water correction for the CRDS values under dry (c) and wet (d) conditions.
900 Panels (e) and (f) show the population density functions.

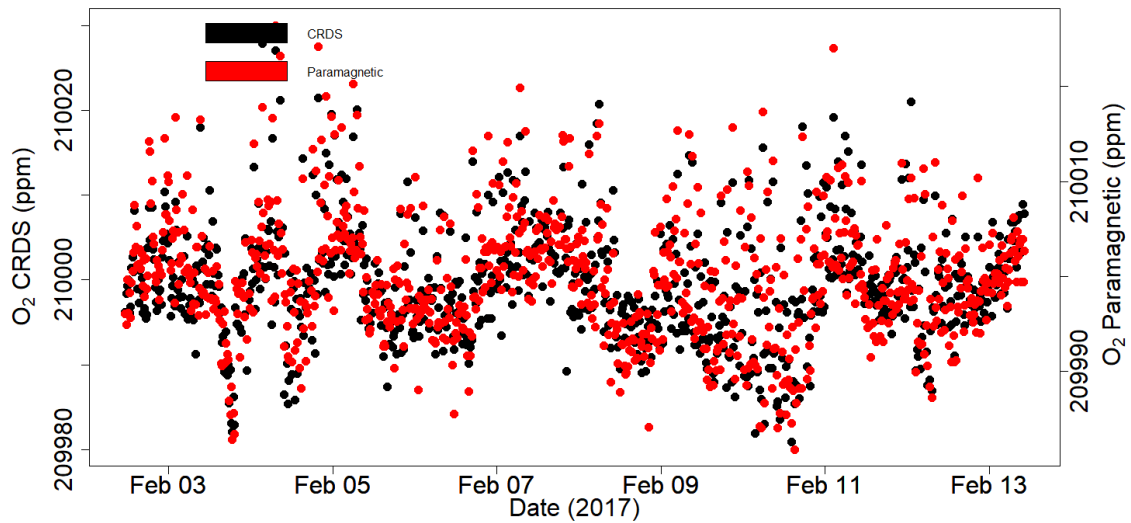
901

902

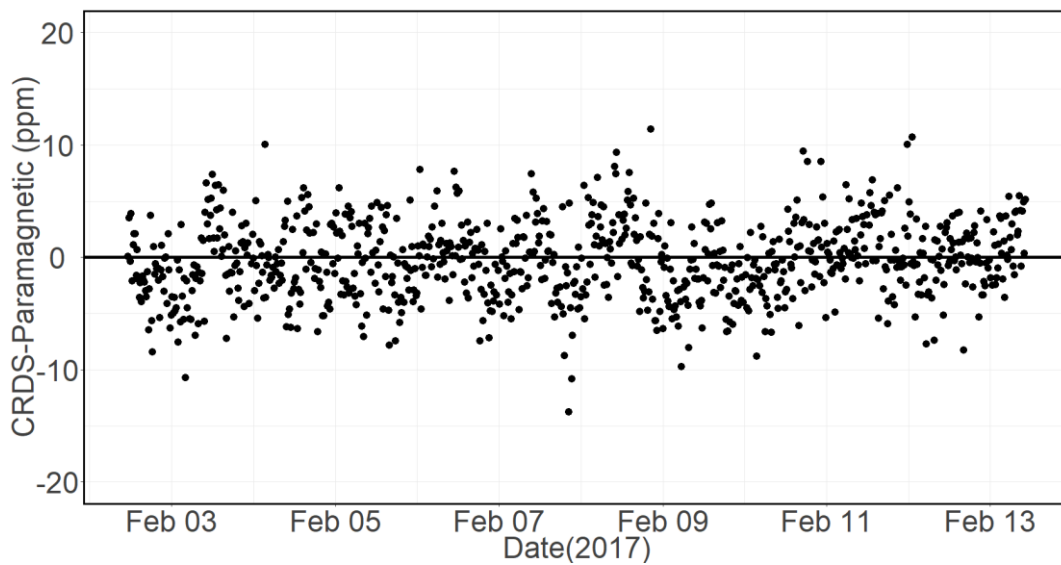
903

904

905



906



907

908 Figure 16. Calibrated ambient air oxygen measurements (1-minute average) at the
 909 Jungfrauoch site using the CRDS and Paramagnetic analyzers both in ppm units (a) and the
 910 absolute difference between the two measurements in ppm (b) by matching time stamps

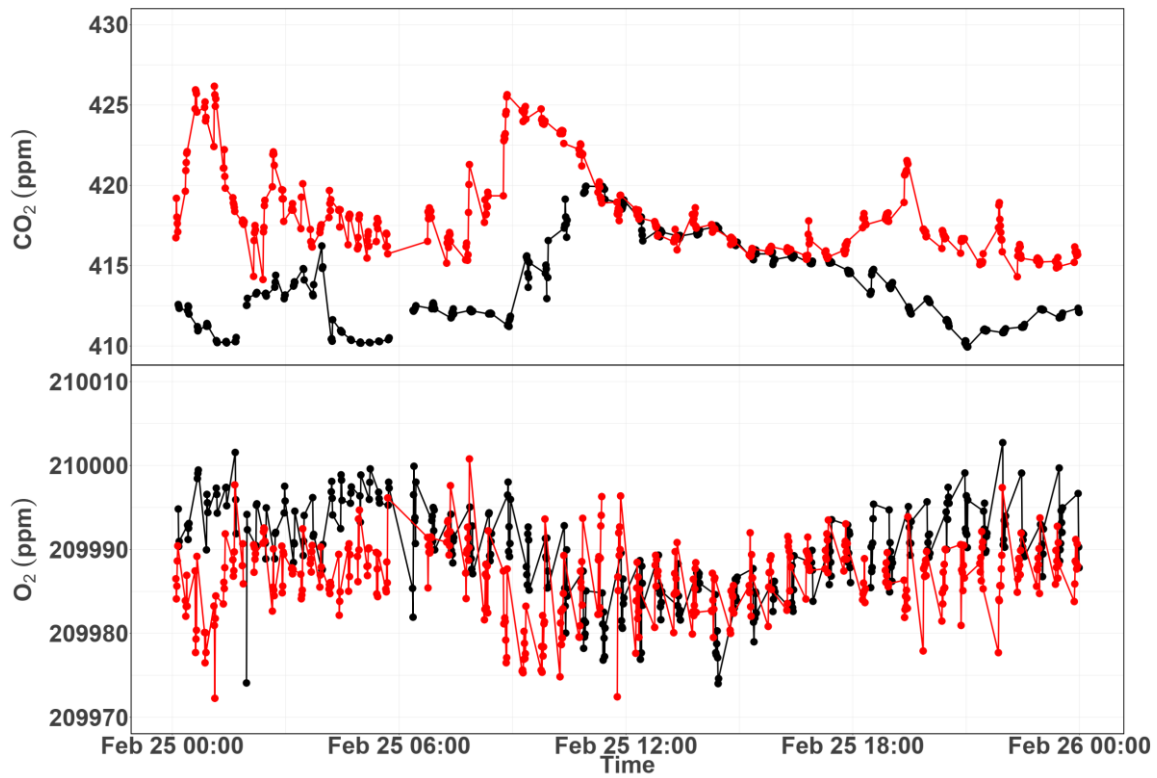
911

912

913

914

915



916

917 Figure 17. Diurnal variations of CO₂ (top) and O₂ (bottom) measurements from the 12 m (red)
 918 and the 212.5 m (black) height levels at Beromünster tower.

919

920

921

922

923

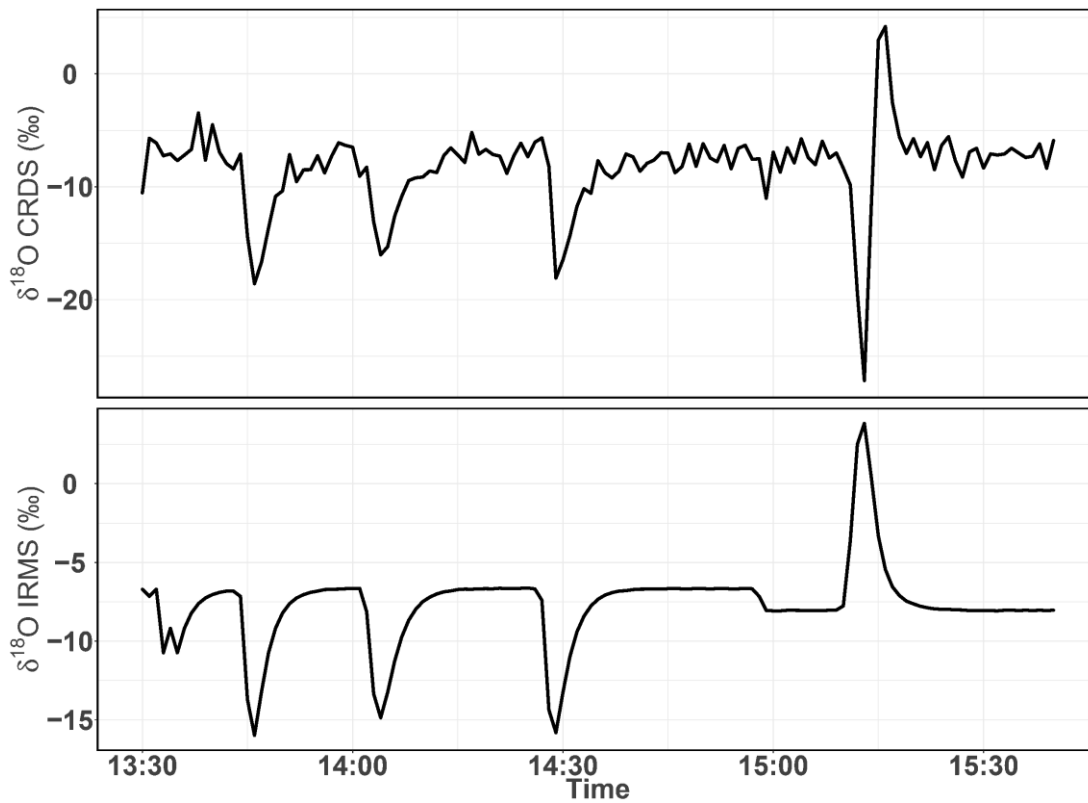
924

925

926

927

928



929

930 Figure 18. Consecutive $\delta^{18}\text{O}$ measurements of a standard gas (CO_2 -free air) filled into three
 931 flasks followed by measurement of breath air using the CRDS analyzer (top) and IRMS
 932 (bottom). These measurements were carried out in the middle of ambient air measurements.

933

934

935

936

937

938

939

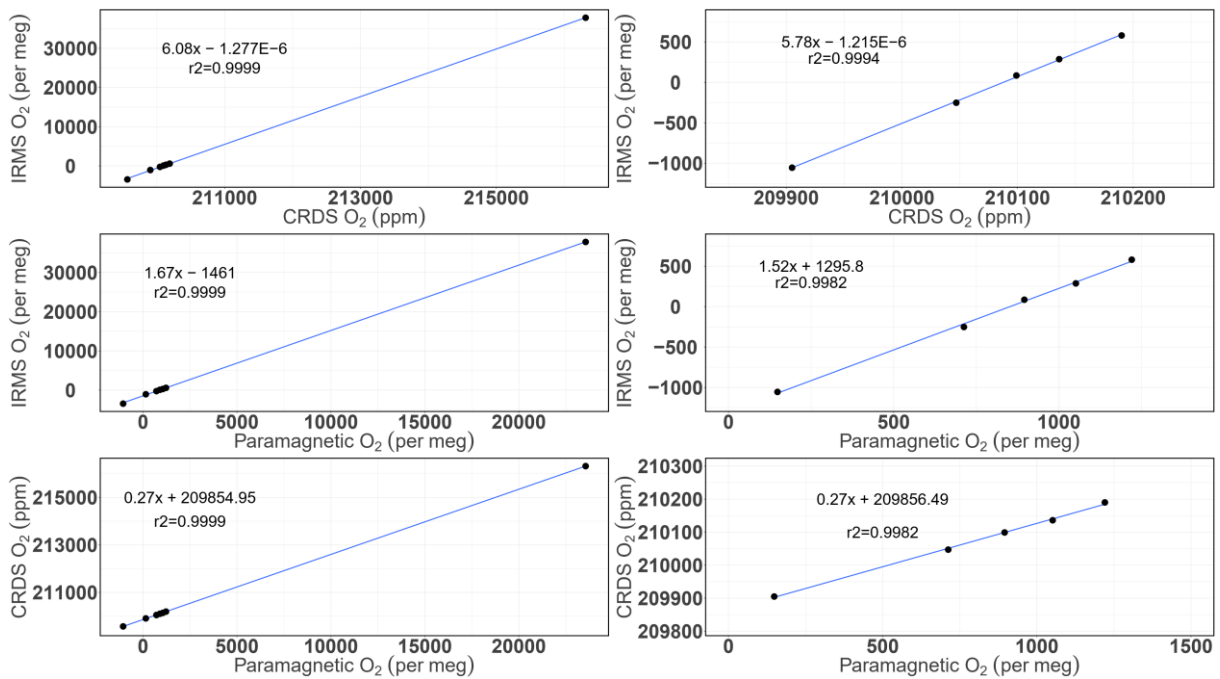
940

941

942

943 **Appendix A.**

944



945

946 Figure A.1. Correlations between the O₂ mixing ratios measured by the CRDS and
 947 Paramagnetic analyzers with the mass spectrometric measurements (uncalibrated values). The
 948 left panels are for all the cylinders measured (standards 1 to 8) while the right ones are after
 949 selecting standards 1-5.

950

951

952

953

954

955

956

957

958 **Appendix B: Uncertainty consideration during mole fraction (ppm) to delta (per meg)**
959 **conversion for air-like gas compositions according to different scenarios**

960 Generally, the Delta notation ($\delta(\text{O}_2/\text{N}_2)$), as given in equation 1 of this publication (also
961 shown below), is used in order to circumvent the influences of dilution by other gas
962 components when determining oxygen mole fractions (Table A1). Yet, several instruments
963 are measuring the oxygen mole fraction such as the paramagnetic cell, the UV-cell as well as
964 the instrument by CRDS analyzer presented here. Therefore, a thorough consideration of the
965 conversion from ppm (mole fraction) to per meg ($\delta(\text{O}_2/\text{N}_2)$ notation) is necessary which is
966 explained in this appendix.

967 Following equation 1 in Thojima et al., 2000, the per meg to ppm conversion has a slope of
968 6.04 if a change only in oxygen is applied as seen in table A2. It changes slightly to 6.11 per
969 meg per ppm, when we talk about nitrogen changes only, or to a slope zero (horizontal line)
970 when talking about any other changes of air components excluding oxygen and nitrogen. The
971 fact that our supplementary plot shows slopes of 5.78 (for the first five standards) or 6.08 per
972 meg per ppm (for all standards except ST-7) is due to a mixed influence dilution effects. The
973 lower slope of 5.78 per meg per ppm documents particularly the influence of the CO₂ dilution
974 effect.

$$\delta\left(\frac{\text{O}_2}{\text{N}_2}\right) (\text{per meg}) = \left(\frac{\left(\frac{\text{O}_2}{\text{N}_2}\right)_{\text{sample}}}{\left(\frac{\text{O}_2}{\text{N}_2}\right)_{\text{reference}}} - 1\right) \cdot 10^6 \quad (1)$$

976 Note that under the assumption the atmospheric N₂ content is constant (i.e. N_{2sample} equals
977 N_{2reference}), we convert relative changes in oxygen given in per meg following equation 1 to
978 oxygen changes in parts per million (equivalent to micromol/mol) by multiplying by the O₂
979 mole fraction (O_{2reference}) expressed as 209500 ppm (the O₂ mole fraction of atmospheric air)

980 (Machta and Hughes, 1970). Hence 1 ppm corresponds approximately to 4.8 per meg, or 1 per
981 meg to $1/4.8$ ($209500/106$) ppm.

982 This is used in our approach since the Picarro instrument measures the O_2 mole fraction which
983 requires to be converted to an O_2/N_2 ratio. Since no information about N_2 is available one
984 assumes a constant value, i.e. N_2 of the standard. Therefore, eq. 1 in the manuscript reduces to
985 $(O_{2,SA}/O_{2,ST}-1) \times 10^6$ or $\Delta O_2/O_{2,ST} \times 10^6$. The value obtained is an estimated $\delta O_{2, \text{norm}}/N_{2, \text{base}}$
986 ratio, which indeed is slightly different from the true $\delta O_{2, \text{norm}}/N_{2, \text{norm}}$. The effect of water
987 dilution (amount of water vapor is measured by the CRDS instrument) is taken into account as
988 described in the manuscript. Yet any other dilution effect is not considered except if
989 additional information is available, e.g. CO_2 concentration measurements. Indeed this dilution
990 effects can be significant and are displayed in the following table A2.

991

992

993

994

995

996

997

998

999

1000 Table A1: Different dilution scenarios and their effect on air-like compositions

Mole fraction	base	original	normalized	original	normalized	original	normalized	original	normalized
N ₂ , ppm	780809	780809	780801.192	780809	780801.192	780809	780801.192	780819	780811.192
O ₂ , ppm	209451	209451	209448.906	209451	209448.906	209461	209458.905	209451	209448.906
Ar, ppm	9340	9340	9339.9066	9350	9349.9065	9340	9339.9066	9340	9339.9066
CO ₂ , ppm	400	410	409.9959	400	399.996	400	399.996	400	399.996
Total	1000000	1000010	1000000	1000010	1000000	1000010	1000000	1000010	1000000
Change		original	apparent	original	apparent	original	apparent	original	apparent
ΔCO ₂ , ppm		10	9.9959	0	-0.0040	0	-0.0040	0	-0.0040
ΔAr, ppm		0	-0.0934	10	9.9065	0	-0.0934	0	-0.0934
ΔO ₂ , ppm		0	-2.0945	0	-2.0945	10	7.9054	0	-2.0945
ΔN ₂ , ppm		0	-7.8080	0	-7.8080	0	-7.8080	10	2.1919

1001

1002 This will lead to the following changes for oxygen, the true and estimated (when N₂ is not

1003 measured) δ(O₂/N₂) ratios and the difference in these δ(O₂/N₂) values.

1004

1005

1006

1007 Table A2: Mole fraction to delta conversion for air-like compositions according to different
 1008 scenarios

Change in ppm		ΔO_2 apparent (change + dilution effect)	$\delta O_{2, \text{norm}}/N_{2, \text{norm}}$ (per meg) ($\delta O_{2, \text{norm}}/N_{2, \text{norm}}/\Delta O_2$ in per meg/ppm) (true)	$\delta O_{2, \text{norm}}/N_{2, \text{base}}$ (per meg) ($\delta O_{2, \text{norm}}/O_{2, \text{base}}/\Delta O_2$ in per meg/ppm) (estimated)	Difference in $\delta O_2/N_2$ (true – estimated) in per meg
ΔCO_2 only	10	-2.0945	0 (0)	-10 (4.77)	10
ΔAr only	10	-2.0945	0 (0)	-10 (4.77)	10
ΔO_2 only	10	7.9054	47.74 (6.04)	37.74 (4.77)	10
ΔN_2 only	10	-2.0946	-12.81 (6.11)	-10 (4.77)	-2.81

1009

1010 $\delta O_{2, \text{norm}}/N_{2, \text{norm}}$: calculated (eg Thojima et al., 2000) or measured for instance by mass
 1011 spectrometry; $\delta O_{2, \text{norm}}/N_{2, \text{base}}$: use fixed conversion factor of 4.77 per meg / ppm based on
 1012 measured O_2 mole fraction (ppm) for instance by the CRDS analyzer.

1013 Incorrectly assumed N_2 , Ar, CO_2 or any additional gas component can lead to changes in the
 1014 estimated $\delta O_2/N_{2, \text{est}}$ values as stated in the table A2. For example a 10 ppm increase in CO_2
 1015 lead to a bias of -10 per meg in $\delta O_{2, \text{norm}}/N_{2, \text{base}}$ compared to the true $\delta O_{2, \text{norm}}/N_{2, \text{norm}}$ value.

1016 This is simply the dilution effect that the increased CO_2 concentration has on the
 1017 corresponding O_2 mole fraction (table A.1) (dilution in oxygen corresponds to the percentage-
 1018 wise assignment of the excess CO_2 in ppm to oxygen, i.e. -10 ppm x oxygen mole fraction =
 1019 2.0946, if O_2 mole fraction corresponds to 0.20946). As can be seen from table A2, addition
 1020 of 10 ppm of N_2 leads to a reduced and opposite effect for the difference in $\delta O_2/N_2$ (true –
 1021 estimated) because the dilution effect on O_2 cannot compensate the change from the increase

1022 in nitrogen, therefore it scales with $-10 \text{ ppm} \times (\text{oxygen mole fraction/nitrogen mole fraction})$.
1023 This also shows that the difference in the Delta values (true – estimated) scales with the
1024 $\delta\text{O}_2/\text{N}_2$ ratio present in the sample. Therefore, best results are obtained when the calibration
1025 gases for which the gas composition is known equals closely the sample gas composition. In
1026 our case this is given – but can certainly be improved – since we are comparing natural air to
1027 air standard. Yet, determinations of the standards that have been used in this study have a
1028 range in N_2 concentrations of -110 to $+110$ ppm for the ST-1 to ST-5, whereas ST-6 ($+700$
1029 ppm) and ST-8 (-6200 ppm) are significantly off compared to our primary standard used for
1030 mass spectrometric determination. Therefore, special attention is required for the precise
1031 determination of standard gas composition and the control of the air sample composition by
1032 means of flask measurements in order to detect potential fractionation effects during air
1033 intake.

1034

1035

1036

1037

1038

1039

1040 **References**

1041 Battle, M., Bender, M. L., Tans, P. P., White, J. W. C., Ellis, J. T., Conway, T., and Francey, R. J.: Global
1042 carbon sinks and their variability inferred from atmospheric O_2 and $\delta^{13}\text{C}$, *Science*, 287, 2467-
1043 2470, 2000.

1044 Bender, M. L., Tans, P. P., Ellis, J. T., Orchardo, J., and Habfast, K.: A High-Precision Isotope Ratio
1045 Mass-Spectrometry Method for Measuring the O-2 N-2 Ratio of Air, *Geochim Cosmochim Ac*, 58,
1046 4751-4758, 1994.

1047 Berhanu, T. A., Satar, E., Schanda, R., Nyfeler, P., Moret, H., Brunner, D., Oney, B., and Leuenberger,
1048 M.: Measurements of greenhouse gases at Beromünster tall tower station in Switzerland, *Atmos.*
1049 *Meas. Tech.* , 9, 2016.

1050 Berhanu, T. A., Szidat, S., Brunner, D., Satar, E., Schanda, R., Nyfeler, P., Battaglia, M., Steinbacher,
1051 M., Hammer, S., and Leuenberger, M.: Estimation of the fossil-fuel component in atmospheric CO2
1052 based on radiocarbon measurements at the Beromünster tall tower, Switzerland, *Atmos. Chem.*
1053 *Phys. Discuss.*, 2017, 1-33, 2017.

1054 Crosson, E. R. J. A. P. B.: A cavity ring-down analyzer for measuring atmospheric levels of methane,
1055 carbon dioxide, and water vapor, 92, 403-408, 2008.

1056 Filges, A., Gerbig, C., Rella, C. W., Hoffnagle, J., Smit, H., KrÄmer, M., Spelten, N., Rolf, C., BozÄki, Z.,
1057 Buchholz, B., and Ebert, V.: Evaluation of the IAGOS-Core GHG Package H2O measurements during
1058 the DENCHAR airborne inter-comparison campaign in 2011, *Atmos. Meas. Tech.*, 11, 5279–5297,
1059 2018, <https://doi.org/10.5194/amt-11-5279-2018>. Gao, F., Zhang, X., Zhang, X., Wang, M., and Wang,
1060 P.: Virtual electronic nose with diagnosis model for the detection of hydrogen and methane in breath
1061 from gastrointestinal bacteria, 28-31 May 2017 2017, 1-3.

1062 Gordon, E., Rothman, S., Hill, C., Kochanov, V., Tan, Y., Bernath, P., Birk, M., Boudon, V., Campargue,
1063 A., Chance, K., Drouin, J., Flaud, J., Gamache, R. R., Hodges, J., Jacquemart, D., Perevalov, I., Perrin, A.,
1064 Shine, P., Smith, M., Tennyson, J., Toon, G., Tran, H., Tyuterev, G., Barbe, A., Császár, G., Devi, M.,
1065 Furtenbacher, T., Harrison, J., Hartmann, J., Jolly, A., Johnson, J., Karman, T., Kleiner, I., Kyuberis, A.
1066 A., Loos, J., Lyulin, M., Massie, S., Mikhailenko, S., Moazzen-Ahmadi, N., Muller, S., Naumenko, O. V.,
1067 Nikitin, A. V., Polyansky, O. L., Rey, M., Rotger, M., Sharpe, S., Sung, K., Starikova, E., Tashkun, S.,

1068 Auwera, J., Wagner, G., Wilzewski, J., Wcisło, P., Yu, S., and Zak, E. J.: The HITRAN2016 molecular
1069 spectroscopic database, 203, 3 - 69, 2017.

1070 Goto, D., Morimoto, S., Ishidoya, S., Aoki, S., and Nakazawa, T.: Terrestrial biospheric and oceanic
1071 CO₂ uptake estimated from long-term measurements of atmospheric CO₂ mole fraction, $\delta^{13}\text{C}$ and
1072 $\delta(\text{O}_2/\text{N}_2)$ at Ny-Ålesund, Svalbard, *Journal of Geophysical Research: Biogeosciences*, doi:
1073 10.1002/2017JG003845, 2017. n/a-n/a, 2017.

1074 Gottlieb, K., Le, C. X., Wachter, V., Sliman, J., Cruz, C., Porter, T., and Carter, S.: Selection of a cut-off
1075 for high- and low-methane producers using a spot-methane breath test: results from a large north
1076 American dataset of hydrogen, methane and carbon dioxide measurements in breath, *Gastroenterol*
1077 *Rep*, 5, 193-199, 2017.

1078 Hartmann, J.-M., Boulet, C., and Robert, D.: *Collisional Effects on Molecular Spectra*, Elsevier Science,
1079 2008.

1080 Henne, S., Brunner, D., Folini, D., Solberg, S., Klausen, J., and Buchmann, B.: Assessment of
1081 parameters describing representativeness of air quality in-situ measurement sites, *Atmos. Chem.*
1082 *Phys.*, 10, 3561-3581, 2010.

1083 Hodges, J. T., Layer, H. P., Miller, W. W., and Scace, G. E.: Frequency-stabilized single-mode cavity
1084 ring-down apparatus for high-resolution absorption spectroscopy, 75, 849-863, 2004.

1085 Keeling, R. F.: Development of an Interferometric Oxygen Analyzer for Precise Measurement of the
1086 Atmospheric O₂ Mole Fraction, UMI, 1988a.

1087 Keeling, R. F.: Measuring correlations between atmospheric oxygen and carbon dioxide mole
1088 fractions: A preliminary study in urban air, *J Atmos Chem*, 7, 153-176, 1988b.

1089 Keeling, R. F. and Manning, A. C.: 5.15 - Studies of Recent Changes in Atmospheric O₂ Content A2 -
1090 Holland, Heinrich D. In: *Treatise on Geochemistry (Second Edition)*, Turekian, K. K. (Ed.), Elsevier,
1091 Oxford, 2014.

1092 Keeling, R. F. and Shertz, S. R.: Seasonal and Interannual Variations in Atmospheric Oxygen and
1093 Implications for the Global Carbon-Cycle, *Nature*, 358, 723-727, 1992.

1094 Keeling, R. F., Stephens, B. B., Najjar, R. G., Doney, S. C., Archer, D., and Heimann, M.: Seasonal
1095 variations in the atmospheric O₂/N₂ ratio in relation to the kinetics of air-sea gas exchange, *Global*
1096 *Biogeochem Cy*, 12, 141-163, 1998.

1097 Lamouroux, J., Sironneau, V., Hodges, J. T., and Hartmann, J. M.: Isolated line shapes of molecular
1098 oxygen: Requantized classical molecular dynamics calculations versus measurements, *Physical*
1099 *Review A*, 89, 042504, 2014.

1100 Le Quéré, C., Andrew, R. M., Friedlingstein, P., Sitch, S., Pongratz, J., Manning, A. C., Korsbakken, J. I.,
1101 Peters, G. P., Canadell, J. G., Jackson, R. B., Boden, T. A., Tans, P. P., Andrews, O. D., Arora, V. K.,
1102 Bakker, D. C. E., Barbero, L., Becker, M., Betts, R. A., Bopp, L., Chevallier, F., Chini, L. P., Ciais, P.,
1103 Cosca, C. E., Cross, J., Currie, K., Gasser, T., Harris, I., Hauck, J., Haverd, V., Houghton, R. A., Hunt, C.
1104 W., Hurtt, G., Ilyina, T., Jain, A. K., Kato, E., Kautz, M., Keeling, R. F., Klein Goldewijk, K., Körtzinger, A.,
1105 Landschützer, P., Lefèvre, N., Lenton, A., Lienert, S., Lima, I., Lombardozzi, D., Metzl, N., Millero, F.,
1106 Monteiro, P. M. S., Munro, D. R., Nabel, J. E. M. S., Nakaoka, S. I., Nojiri, Y., Padín, X. A., Pregon, A.,
1107 Pfeil, B., Pierrot, D., Poulter, B., Rehder, G., Reimer, J., Rödenbeck, C., Schwinger, J., Séférian, R.,
1108 Skjelvan, I., Stocker, B. D., Tian, H., Tilbrook, B., van der Laan-Luijkx, I. T., van der Werf, G. R., van
1109 Heuven, S., Viovy, N., Vuichard, N., Walker, A. P., Watson, A. J., Wiltshire, A. J., Zaehle, S., and Zhu,
1110 D.: Global Carbon Budget 2017, *Earth Syst. Sci. Data Discuss.*, 2017, 1-79, 2017.

1111 Machta, L. and Hughes, E.: Atmospheric Oxygen in 1967 to 1970, *Science*, 168, 3939, 1582-1584,
1112 1970.

1113 Manning, A.: Temporal variability of atmospheric oxygen from both continuous and measurements
1114 and a flask sampling network: tools for studying the global carbon cycle, Ph.D. Ph.D., University of
1115 California, San Diego, San Diego, California, USA, 2001.

1116 Manning, A. C. and Keeling, R. F.: Global oceanic and land biotic carbon sinks from the Scripps
1117 atmospheric oxygen flask sampling network, *Tellus B*, 58, 95-116, 2006.

1118 Manning, A. C., Keeling, R. F., and Severinghaus, J. P.: Precise atmospheric oxygen measurements
1119 with a paramagnetic oxygen analyzer, *Global Biogeochem Cy*, 13, 1107-1115, 1999.

1120 Marrero, T. R. and Mason, E. A.: Gaseous Diffusion Coefficients, *Journal of Physical and Chemical*
1121 *Reference Data* 1, 3, 1972.

1122 Martin, N. A., Ferracci, V., Cassidy, N., and Hoffnagle, J. A. J. A. P. B.: The application of a cavity ring-
1123 down spectrometer to measurements of ambient ammonia using traceable primary standard gas
1124 mixtures, 122, 219, 2016.

1125 McKay, L. F., Eastwood, M. A., and Brydon, W. G.: Methane Excretion in Man - a Study of Breath,
1126 Flatus, and Feces, *Gut*, 26, 69-74, 1985.

1127 Nevison, C. D., Keeling, R. F., Kahru, M., Manizza, M., Mitchell, B. G., and Cassar, N.: Estimating net
1128 community production in the Southern Ocean based on atmospheric potential oxygen and satellite
1129 ocean color data, *Global Biogeochem Cy*, 26, 2012.

1130 Oney, B., Henne, S., Gruber, N., Leuenberger, M., Bamberger, I., Eugster, W., and Brunner, D.: The
1131 CarboCount CH sites: characterization of a dense greenhouse gas observation network, *Atmos.*
1132 *Chem. Phys.*, 15, 11147-11164, 2015.

1133 Press, W. H., Teukolsky, S. A., Vetterling, W. T., and Flannery, B. P.: *Numerical Recipes 3rd Edition:*
1134 *The Art of Scientific Computing*, Cambridge Printing Press, Cambridge, England, 1986.

1135 Press, W. H., Teukolsky, S. A., Vetterling, W. T., and Flannery, B. P.: *Numerical recipes in C: the art of*
1136 *scientific computing*, Cambridge University Press, London, 1992.

1137 Ryter, S. W. and Choi, A. M. K.: Carbon monoxide in exhaled breath testing and therapeutics, *J Breath*
1138 *Res*, 7, 2013.

1139 Satar, E., Berhanu, T. A., Brunner, D., Henne, S., and Leuenberger, M.: Continuous CO₂/CH₄/CO
1140 measurements (2012–2014) at Beromünster tall tower station in Switzerland, *Biogeosciences*, 13,
1141 2623-2635, 2016.

1142 Schibig, M. F., Steinbacher, M., Buchmann, B., van der Laan-Luijkx, I. T., van der Laan, S., Ranjan, S.
1143 and Leuenberger, M. C.: Comparison of continuous in situ CO₂ observations at Jungfrauoch using
1144 two different measurement techniques, *Atmospheric Measurement Techniques*
1145 , 8, 57-68, 10.5194/amt-8-57-2015, 2015.

1146 Severinghaus, J. P.: Studies of the terrestrial O₂ and carbon cycles in sand dune gases and in
1147 Biosphere Doctoral Ph.D., Columbia University, New York, USA, 1995.

1148 Steig, E. J., Gkinis, V., Schauer, A. J., Schoenemann, S. W., Samek, K., Hoffnagle, J., Dennis, K. J., and
1149 Tan, S. M.: Calibrated high-precision ¹⁷O-excess measurements using cavity ring-down
1150 spectroscopy with laser-current-tuned cavity resonance, *Atmos. Meas. Tech.*, 7, 2014.

1151 Stephens, B. B., Bakwin, P. S., Tans, P. P., Teclaw, R. M., and Baumann, D. D.: Application of a
1152 differential fuel-cell analyzer for measuring atmospheric oxygen variations, *J Atmos Ocean Tech*, 24,
1153 82-94, 2007.

1154 Sturm, P., Leuenberger, M., Valentino, F.L., Lehmann, B. and B. Ihly: Measurements of CO₂, its stable
1155 isotopes, O₂/N₂, and ²²²Rn at Bern, Switzerland, *Atmospheric Chemistry and Physics*, 6, 1991-2004,
1156 2006.

1157 Tan, Y., Kochanov, R.V., Rothman, L., and Gordon, I.E.: Introduction of water-vapor broadening
1158 coefficients and their temperature dependence exponents into the HITRAN database, Part 1: CO₂,
1159 N₂O, CO, CH₄, O₂, NH₃, and H₂S, Submitted to *Journal of Geophysical Research Atmospheres*, 2019,
1160 [arXiv:1906.01475](https://arxiv.org/abs/1906.01475).

1161 Tennyson, J., Bernath, P. F., Campargue, A., Császár, A. G., Daumont, L., Gamache, R. R., Hodges, J. T.,
1162 Lisak, D., Naumenko, O. V., Rothman, L. S., Tran, H., Zobov, N. F., Buldyreva, J., Boone, C. D., De Vizia,

1163 M. D., Gianfrani, L., Hartmann, J.-M., McPheat, R., Weidmann, D., Murray, J., Ngo, N. H., and
1164 Polyansky, O. L.: Recommended isolated-line profile for representing high-resolution spectroscopic
1165 transitions (IUPAC Technical Report), 86, 1931–1943, 2014.

1166 Tohjima, Y.: Method for measuring changes in the atmospheric O₂/N₂ ratio by a gas
1167 chromatograph equipped with a thermal conductivity detector, *J Geophys Res-Atmos*, 105, 14575-
1168 14584, 2000.

1169 Tran, H., Turbet, M., Hanoufa, S., Landsheere, X., Chelin, P., Ma, Q., Hartmann, J.: The CO₂-
1170 broadened H₂O continuum in the 100–1500 cm⁻¹ region: Measurements, predictions and empirical
1171 model, *Journal of Quantitative Spectroscopy and Radiative Transfer*, 230, 75-80, 2019.

1172 Valentino, F. L., Leuenberger, M., Uglietti, C., and Sturm, P.: Measurements and trend analysis of O₂,
1173 CO₂ and δ¹³C of CO₂ from the high altitude research station Junfgraujoch, Switzerland — A
1174 comparison with the observations from the remote site Puy de Dôme, France, *Sci Total Environ*, 391,
1175 203-210, 2008.

1176 Varghese, P. L. and Hanson, R. K.: Collisional narrowing effects on spectral line shapes measured at
1177 high resolution, *Appl. Opt.*, 23, 2376-2385, 1984.

1178 Wójtewicz, S., Cygan, A., Masłowski, P., Domysławska, J., Wcisło, P., Zaborowski, M., Lisak, D.,
1179 Trawiński, R. S., and Ciuryło, R.: Spectral line-shapes of oxygen B-band transitions measured with
1180 cavity ring-down spectroscopy, *Journal of Physics: Conference Series*, 548, 012028, 2014.

1181 Wolf, P. G., Parthasarathy, G., Chen, J., O'Connor, H. M., Chia, N., Bharucha, A. E., and Gaskins, H. R.:
1182 Assessing the colonic microbiome, hydrogenogenic and hydrogenotrophic genes, transit and breath
1183 methane in constipation, *Neurogastroent Motil*, 29, 2017.

1184 Zellweger, C., Forrer, J., Hofer, P., Nyeki, S., Schwarzenbach, B., Weingartner, E., Ammann, M., and
1185 Baltensperger, U.: Partitioning of reactive nitrogen (NO_y) and dependence on
1186 meteorological conditions in the lower free troposphere, *Atmos. Chem. Phys.*, 3, 779-796, 2003.

